

# **PROPAGATION OF REGIONAL PHASES AND THEIR CODAS IN SOUTHERN ASIA AND THE MIDDLE EAST**

Lianli Cong  
Brian J. Mitchell

St Louis University  
Department of Earth and Atmospheric Sciences  
3507 Laclede Avenue  
St. Louis, MO 63103

17 November 1997

Final Report  
12 June 1995 - 11 June 1997

19980602 024

approved for public release; distribution unlimited



DEPARTMENT OF ENERGY  
Office of Non-Proliferation  
and National Security  
WASHINGTON, DC 20585




AIR FORCE RESEARCH LABORATORY  
Space Vehicles Directorate  
29 Randolph Road  
AIR FORCE MATERIEL COMMAND  
HANSCOM AFB, MA 01731-3010


SPONSORED BY  
Department of Energy  
Office of Non-Proliferation and National Security

MONITORED BY  
Air Force Research Laboratory  
CONTRACT No. F19628-95-K-0004

The views and conclusions contained in this document are those of the authors and should not be interpreted as representing the official policies, either express or implied, of the Air Force or U.S. Government.

This technical report has been reviewed and is approved for publication.

  
KATHARINE KADINSKY-CADE  
Contract Manager

  
CHARLES P. PIKE, Deputy Director  
Integration and Operations Division

This report has been reviewed by the ESD Public Affairs Office (PA) and is releasable to the National Technical Information Service (NTIS).

Qualified requestors may obtain copies from the Defense Technical Information Center. All others should apply to the National Technical Information Service.

If your address has changed, or you wish to be removed from the mailing list, or if the addressee is no longer employed by your organization, please notify AFRL/VSOE, 29 Randolph Road, Hanscom AFB, MA 01731-3010. This will assist us in maintaining a current mailing list.

Do not return copies of the report unless contractual obligations or notices on a specific document requires that it be returned.

## REPORT DOCUMENTATION PAGE

Form Approved  
OMB No. 0704-0186

Public reporting burden for this collection of information is estimated to average 1 hour per response, including the time for reviewing instructions, searching existing data sources, gathering and maintaining the data needed, and completing and reviewing the collection of information. Send comments regarding this burden estimate or any other aspect of this collection of information, including suggestions for reducing this burden, to Washington Headquarters Services, Directorate for Information Operations and Reports, 1215 Jefferson Davis Highway, Suite 1204, Arlington, VA 22202-4302, and to the Office of Management and Budget, Paperwork Reduction Project (0704-0186), Washington, DC 20503.

|  |   |   |                                   |
|--|---|---|-----------------------------------|
| 1. AGENCY USE ONLY (Leave blank)   | 2. REPORT DATE<br>11/17/97                                  | 3. REPORT TYPE AND DATES COVERED<br>Final Report 6/12/95 - 6/11/97      |                                   |
| 4. TITLE AND SUBTITLE<br>Propagation of Regional Phases and Their Codas in Southern Asia and the Middle East   |   | 5. FUNDING NUMBERS<br>F19628-95-K-0004<br>PE 69120H<br>PRDENN TAGM WUAE |                                   |
| 6. AUTHOR(S)<br>Lianli Cong<br>Brian J. Mitchell   |   |   |                                   |
| 7. PERFORMING ORGANIZATION NAME(S) AND ADDRESS(ES)<br>Dept. of Earth and Atmospheric Sciences<br>Saint Louis University<br>3507 Laclede Avenue<br>St. Louis, MO 63103  |   | 8. PERFORMING ORGANIZATION<br>REPORT NUMBER                             |                                   |
| 9. SPONSORING/MONITORING AGENCY NAME(S) AND ADDRESS(ES)<br>Air Force Research Laboratory<br>29 Randolph Road<br>Hanscom AFB, MA 01731-3010<br>Contract Manager: Katharine Kadinsky-Cade/VSBS   |   | 10. SPONSORING/MONITORING<br>AGENCY REPORT NUMBER<br>PL-TR-97-2148      |                                   |
| 11. SUPPLEMENTARY NOTES<br>This research was sponsored by the Department of Energy, Office of Non-Proliferation and National Security, Washington, DC 20585  |   |   |                                   |
| 12a. DISTRIBUTION/AVAILABILITY STATEMENT<br>Approved for public release. Distribution unlimited.   |   | 12b. DISTRIBUTION CODE  |                                   |
| 13. ABSTRACT (Maximum 200 words)<br>Observed velocities and attenuation of fundamental-mode Rayleigh waves in the period range 7-82 sec were inverted for shear-wave velocity and shear-wave Q structure in the Middle East using a two-station method. Additional information on Q structure variation within each region was obtained by studying amplitude spectra of fundamental-mode and higher-mode Rayleigh waves. We obtained models for the Turkish and Iranian Plateaus (Region 1), areas surrounding and including the Black and Caspian Seas (Region 2), and the Arabian Peninsula (Region 3). The effect of continent-ocean boundaries and mixed paths in Region 2 may lead to unrealistic features in the models obtained there. Shear velocities vary significantly in the uppermost 10 km of the crust, being 3.21, 2.85, and 3.39 km/s for Regions 1, 2, and 3, respectively. Q's for the upper 10 km of the crust are 63, 71, and 201 for Regions 1, 2, and 3, respectively. Crustal Q's at 30 km depth for the three regions are about 51, 71, and 134. The lower crustal Q values contrast sharply with results from stable continental regions where shear-wave Q may be as high as a thousand or more. |   |   |                                   |
| 14. SUBJECT TERMS<br>Attenuation, Rayleigh waves, Q, Middle East   |   | 15. NUMBER OF PAGES<br>64   |                                   |
|  |   | 16. PRICE CODE  |                                   |
| 17. SECURITY CLASSIFICATION<br>OF REPORT<br>Unclassified   | 18. SECURITY CLASSIFICATION<br>OF THIS PAGE<br>Unclassified | 19. SECURITY CLASSIFICATION<br>OF ABSTRACT<br>Unclassified              | 20. LIMITATION OF ABSTRACT<br>SAR |

## Table of Contents

|  |    |
|--|----|
| Abstract   | 1  |
| Introduction   | 2  |
| Overview of Middle East Tectonics                            | 3  |
| Previous Seismological Work in the Middle East               | 5  |
| Regionalization and Data Acquisition                         | 6  |
| Interstation Group and Phase Velocities                      | 10 |
| Shear Velocity Models Obtained Using the Two-station Method  | 20 |
| Shear-wave Q Models Obtained Using the Two-station Method    | 30 |
| Shear-wave Q Models Obtained Using the Single-station Method | 37 |
| Discussion   | 48 |
| Conclusions  | 49 |
| Acknowledgments  | 51 |
| References   | 52 |

## List of Figures

| Figure |  | Page |
|--------|--|------|
| 1      | Tectonic map (modified from Seber <i>et al.</i> , 1997) showing the relative movement of the plates in the Middle East, the major tectonic features, and the tectonic provinces in the Arabian plate. Shading delineates the Arabian Shield (lighter), and the Turkish and Iranian Plateaus (darker). For the latter region, only elevations higher than 1500 m are shaded.  | 4    |
| 2      | Paths used for two-station determinations of interstation group and phase velocities and attenuation. Triangles denote stations and circles indicate earthquakes used. Numbers refer to the events described in Table 2.   | 7    |
| 3      | Paths used for single-station studies of multi-mode Rayleigh-wave attenuation. The meanings of the symbols are explained in the caption for Figure 2. Numbers refer to the events described in Table 3.  | 8    |
| 4      | (Top) Original trace (in counts) for the earthquake that occurred on January 28, 1996 as recorded at station SODA. (Bottom) Windowed trace of ground displacement after correction for geometrical spreading and instrument response, and bandpass filtering with corner frequencies of 0.01 and 1 Hz.   | 12   |
| 5      | Contoured spectral amplitudes of fundamental- and higher-mode Rayleigh waves obtained for an earthquake that occurred on 22 April 1995 and recorded at station GNI. The windowed ground displacement, after correction for the geometrical spreading and instrument response, and bandpass filtering, is displayed at the rightmost part of the figure. The same trace with a linear group velocity scale is plotted adjacent to the dispersion diagram. | 13   |
| 6      | Interstation group (bottom) and phase (top) velocities for the station pairs in Region 1. The caption shows symbols used for various station pairs. Phase velocities are given on the ordinate on the right side of the plots, whereas group velocities are given on the left ordinate on the left.  | 15   |
| 7      | Interstation group (bottom) and phase (top) velocities for the station pairs in Region 2. See the caption for Figure 6.  | 16   |
| 8      | Interstation group (bottom) and phase (top) velocities for the station pairs in Region 3. See the caption for Figure 6.  | 17   |
| 9      | Interstation group (bottom) and phase (top) velocities for the station pair ABKT-BGIO.   | 19   |

|    |  |    |
|----|--|----|
| 10 | Shear-velocity model and resolving kernels for Region 1. The dashed line indicates the starting model. The horizontal lines indicate the error estimates for the models. Narrow resolving kernels centered at the given depths indicate good resolution whereas broad kernels indicate poorer resolution.  | 21 |
| 11 | Group and phase velocities, and predicted dispersion curves for Region 1. The vertical lines indicate one standard deviation.  | 23 |
| 12 | Shear-velocity models for the three regions. The horizontal lines indicate the error estimates for the models.   | 24 |
| 13 | Comparison of the shear-velocity model for the Arabian Peninsula with those from other studies in the same region.   | 26 |
| 14 | Comparison of the shear-velocity model for the Turkish and Iranian Plateaus with those from other studies in the same region.  | 28 |
| 15 | Velocity models for the three regions of this study obtained using different initial values. For Region 2 (middle) and 3 (right) the abscissas are displaced for clarity.  | 29 |
| 16 | Rayleigh-wave attenuation determined for paths in Region 3. The caption shows symbols used for various station pairs.  | 31 |
| 17 | Shear-wave $Q$ model and resolving kernels for Region 3. See the caption for Figure 10.  | 32 |
| 18 | Observed (circles) and predicted (line) attenuation coefficients for Region 3. The vertical lines indicate one standard deviation.   | 33 |
| 19 | Shear-wave $Q$ models for the three regions. The horizontal lines indicate the error estimates for the models.   | 34 |
| 20 | Shear-wave $Q$ models of the three regions of this study obtained using different initial values. See the caption for Figure 15.   | 36 |
| 21 | An example showing the determination of shear-wave $Q$ in each layer. (a) $Q_\mu$ varies in layer 1. (b) Using the best value (70) for layer 1, $Q_\mu$ is varied in layer 2. (c) Using the best values in layer 1 (70) and layer 2 (50), $Q_\mu$ is varied in layer 3. (d) Using the best values in layer 1 (70), layer 2 (50), and layer 3 (90), $Q_\mu$ is varied in layer 4. | 38 |
| 22 | Shear-wave $Q$ models for the three regions obtained using the single-station method (light lines) compared to models obtained using the two-station method (heavy lines). The four models for Region 1 are for paths indicated in Figure 23, and the three models for Region 3 are for the paths indicated in Figure 25.  | 41 |

|    |  |    |
|----|--|----|
| 23 | Comparison of theoretical multi-mode spectra for models of Region 1 with observed spectra. Fundamental-mode observations are shown with open symbols and higher-mode observations are denoted by closed symbols. | 42 |
| 24 | Comparison of theoretical fundamental-mode spectra for models of Region 2 with observed spectra. Higher modes are not observed in this region.   | 43 |
| 25 | Same as Figure 23, but for Region 3.   | 44 |

### List of Tables

| Table |   | Page |
|-------|---|------|
| 1     | Station information                                     | 9    |
| 2     | Earthquakes studied using the two-station method        | 10   |
| 3     | Earthquakes studied using the single-station method     | 11   |
| 4     | $Q_\mu$ models obtained using the single-station method | 40   |

## Abstract

Observed velocities and attenuation of fundamental-mode Rayleigh waves in the period range 7-82 sec were inverted for shear-wave velocity and shear-wave  $Q$  structure in the Middle East using a two-station method. Additional information on  $Q$  structure variation within each region was obtained by studying amplitude spectra of fundamental-mode and higher-mode Rayleigh waves. We obtained models for the Turkish and Iranian Plateaus (Region 1), areas surrounding and including the Black and Caspian Seas (Region 2), and the Arabian Peninsula (Region 3). The effect of continent-ocean boundaries and mixed paths in Region 2 may lead to unrealistic features in the models obtained there. At lower crustal and upper-mantle depths, shear velocities are similar in all three regions. Shear velocities vary significantly in the uppermost 10 km of the crust, being 3.21, 2.85, and 3.39 km/s for Regions 1, 2, and 3, respectively.  $Q$  models obtained from an inversion of interstation attenuation data show that crustal shear-wave  $Q$  is highest in Region 3 and lowest in Region 1.  $Q$ 's for the upper 10 km of the crust are 63, 71, and 201 for Regions 1, 2, and 3, respectively. Crustal  $Q$ 's at 30 km depth for the three regions are about 51, 71, and 134. The lower crustal  $Q$  values contrast sharply with results from stable continental regions where shear-wave  $Q$  may be as high as a thousand or more. These low values may indicate that fluids reside in faults, cracks, and permeable rock at lower crustal, as well as upper crustal depths due to convergence and intense deformation at all depths in the Middle Eastern crust.



## 1. Introduction

Seismic surface waves have been widely used to study the shear-wave velocity distribution in the Earth. In recently years, high-quality data and increasing numbers of favorably located, modern, digital stations have enabled seismologists to apply tomographic techniques to surface dispersion data. Numerous such studies have provided information of regional shear-velocity variations at both global and regional scales in the Earth.

Studies of surface-wave attenuation have been less numerous mainly because of well-known difficulties in measurement; surface waves may be contaminated by lateral refraction and multipathing that may focus or defocus energy and produce spurious results. It is, however, important to study attenuation because it can provide information on temperature, fluid content, phase change, and density of solid-state defects in the crust and mantle, phenomena that are not easily studied using only seismic wave velocities.

Few models of shear-wave  $Q$  ( $Q_\mu$ ) in the crust and upper mantle have been obtained for continental regions. But these have given us some information on low  $Q_\mu$  related to the tectonic history of various regions (Mitchell, 1995). That work suggested that the value of  $Q_\mu$  obtained in the upper crust of any region is directly proportional to the time that has elapsed since the most recent episode of major tectonic activity there.

The present study measures Rayleigh-wave dispersion and attenuation in the Middle East, a complex region of interaction between the Eurasian, Arabian, and African plates. We will invert two-station data for models of shear velocity ( $\beta$ ) and  $Q_\mu$  for three broad regions and study smaller-scale variations of  $Q_\mu$  within each region using a single-station method. The  $Q_\mu$  models will then be compared to the geology and tectonic history of different portions of the Middle East.

## 2. Overview of Middle East Tectonics

The Middle East is a tectonically complex region where the Arabian, African, and Eurasian plates meet. Figure 1 shows the relative movement of the plates, the major tectonic features, and the boundaries of tectonic provinces in that region.

The Arabian plate, consisting of a shield in the west, a central shelf, and platform and basins in the east, is the most stable portion in this region. It is bounded on the northwest by the Dead Sea and East Anatolian faults, and on the northeast by the Zagros thrust belt. The North Anatolian fault extends in an east-west direction across almost all of Turkey. The Arabian shield consists predominantly of Precambrian gneiss and metamorphosed sedimentary and volcanic rocks that have been intruded by granites (Powers *et al.*, 1966; Brown, 1972). The thin basaltic lava flows that have been emplaced along the western border of the shield since Miocene time reflect the intensity of volcanism in the region (Brown, 1972; Coleman, 1977, Mokhtar and Al-Saeed, 1994). East of the shield, the shelf is tectonically stable. A cross-section through the peninsula (Seber *et al.*, 1997), trending roughly east-west, shows that the thickness of the sediments increases gradually across the shelf area, more rapidly to the east, reaching about 10 km in the basin region.

The Arabian plate and Eurasian plate are currently colliding along the Zagros suture zone in western Iran (Stocklin, 1974; Sengör and Kidd, 1979; Stoneley, 1981). The Turkish and Iranian Plateaus, resulting from the collision between the Arabian and Eurasian plates, are about 1500 km high in average (Sengör and Kidd, 1979). After continental collision during the late Miocene, convergence between Arabia and Eurasia is continuing as shown by the Pliocene to recent folding and thrusting in the Zagros, the border folds of southeastern Turkey (Ketin, 1966), and the present diffuse seismicity of the entire Turkish and Iranian Plateaus (Canitez and Ucer, 1967; McKenzie, 1972; Nowroozi, 1972; Berberian, 1976).

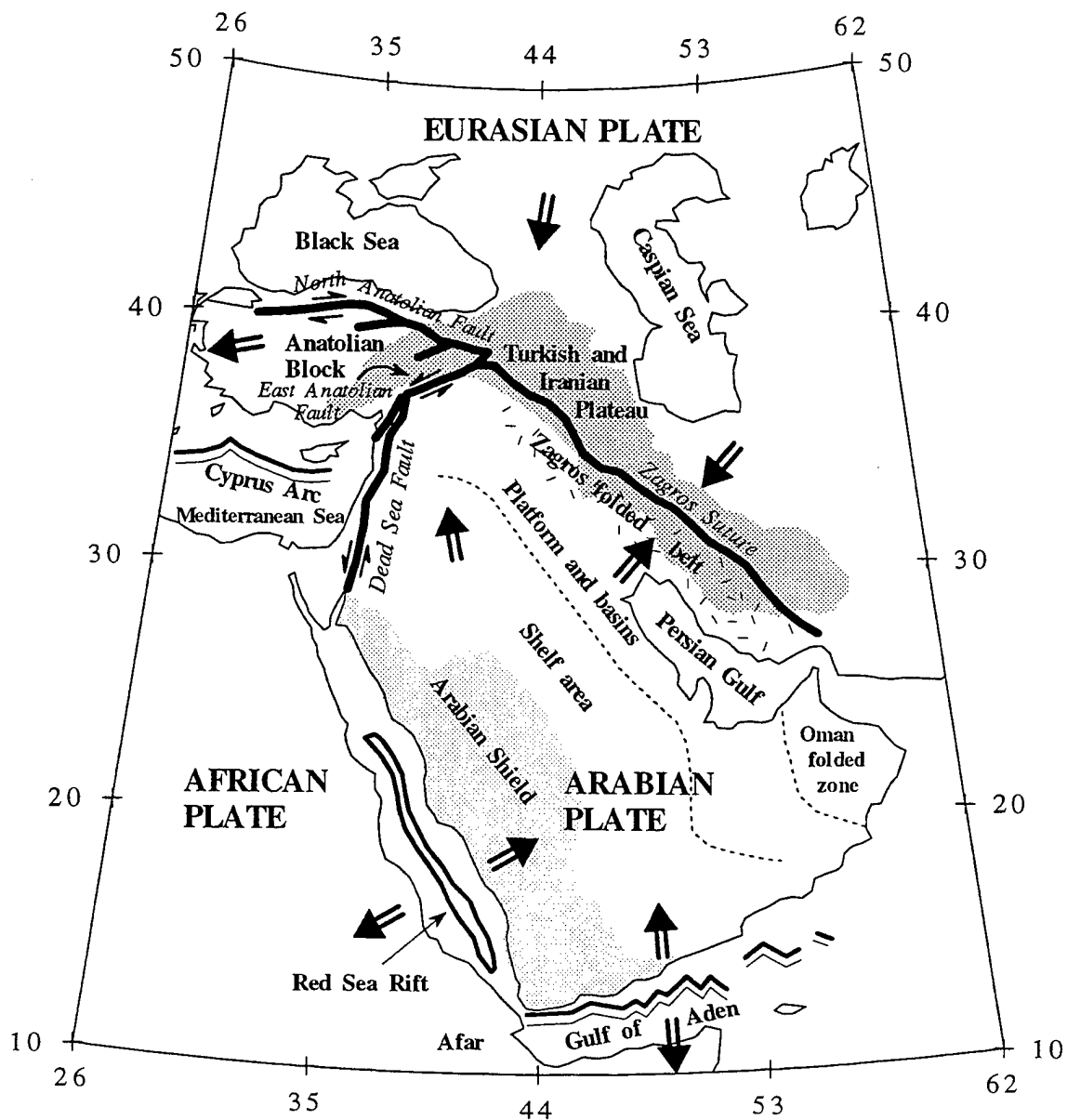


Figure 1

### 3. Previous Seismological Work in the Middle East

Although the tectonics of the Middle East is well understood, only a few reliable models of shear velocity and attenuation have been obtained there. In an early study, Niazi (1968) inverted short-period surface-wave group and phase velocities, and obtained shear velocities of 3.4 km/s for the upper crust, 3.6 km/s for the lower crust and 4.6-4.9 km/s for the upper mantle in the Arabian Peninsula. Knopoff and Fouda (1975) inverted the phase velocities of Rayleigh waves for the period range 22-167 sec to obtain shear velocity models using a two-station method. The paths connecting station pairs (SHI-HLW and SHI-JER) are both located in the northern part of the peninsula, trending east-west. Their study showed a variety of solutions which can explain the data. Mokhtar and Al-Saeed (1994) inverted group velocities of fundamental- and higher-mode Rayleigh and Love waves for velocity structure in the Arabian Peninsula. They studied paths between many epicenters and station RYD, located in the center of Arabian Peninsula. They divided their data into three major groups and obtained different models for each group. Ghalib (1992) used data recorded at stations in the northern part of the Arabian Peninsula to invert for the velocity structure. The only models of velocity structure known for the Turkish Plateau are those obtained by Mindevalli and Mitchell (1989) using the single-station measurements of Rayleigh and Love wave group velocities in the period range 8-50 sec. Different models were obtained for eastern and western Turkey. In this study, detailed velocity models will be provided for different regions of the Middle East.

$Q$  studies in the Middle East have indicated that both regional phases and surface waves attenuate rapidly with distance. Kadinsky-Cade *et al.* (1981) found that regional phases were extinguished along some paths, but not along others. Numerical values for  $L_g Q$  in Iran were obtained by Nuttli (1980) and by Jih and Lynnes (1992). Both studies indicate that  $L_g Q$  is low in that region, and the latter study showed that it is also quite variable for different paths across the Iranian Plateau. Seber and Mitchell (1992) inverted surface wave attenuation data

to obtain the  $Q_\mu$  models for the upper crust of the Arabian Peninsula. They found that shear-wave  $Q$  values in the crust vary from about 60 along the margin of Red Sea to 100-150 in the central part of the peninsula; and 65-80 in the eastern folded region. Ghalib (1992) applied the extended coda- $Q$  technique to short-period  $L_g$  coda waves, obtaining a uniform distribution of  $L_g$  coda  $Q$  with an average value of 214 for the Arabian plate.

#### **4. Regionalization and Data Acquisition**

In this study, we used both two- and single-station methods for both velocity and attenuation studies. In order to model the regional variation of shear velocities and attenuation in the Middle East, we have divided it into three regions, based upon the availability of data for two-station studies. Region 1 consists of the Turkish and Iranian Plateaus and includes the station pairs GNI-KIV and GNI-ANTO (Figure 2). Those paths are confined strictly to continents. Paths crossing the Black and Caspian Seas are excluded from this region and are assigned to Region 2. The station pairs for that region are ANTO-KIV, GNI-ABKT, and KIV-ABKT that cover the two seas plus a large land area around them. Region 3 is the Arabian Peninsula. For that region we used data from stations within Saudi Arabia as well as one station in Israel. The station pairs for Region 3 are BGIO-RAYN, BGIO-HALM, AFIF-SODA, HALM-RANI, and HALM-SODA.

To improve regional coverage we used a multi-mode method that requires only a single station (Cheng and Mitchell, 1981). Figure 3 shows the additional paths and improved regional coverage made possible by the single-station method.

The stations used in this study include four Incorporated Research Institution for Seismology (IRIS) stations (ANTO, ABKT, GNI, KIV), one Geophone station (BGIO), and five stations in Saudi Arabia (RANI, RAYN, HALM, AFIF, SODA), deployed temporarily by the University of California at San Diego and Boise State University. The locations of the stations are given in Table 1. All of

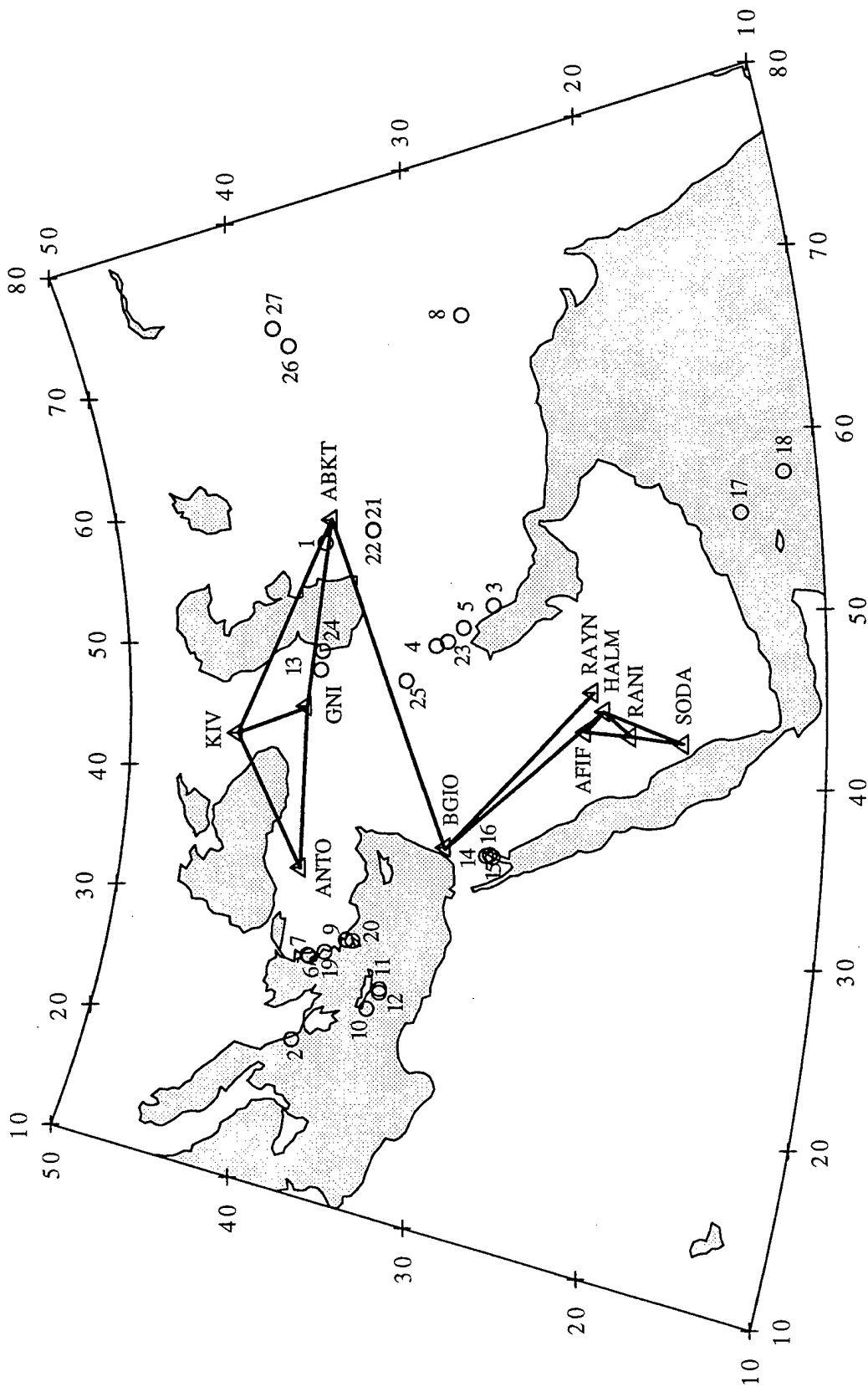


Figure 2

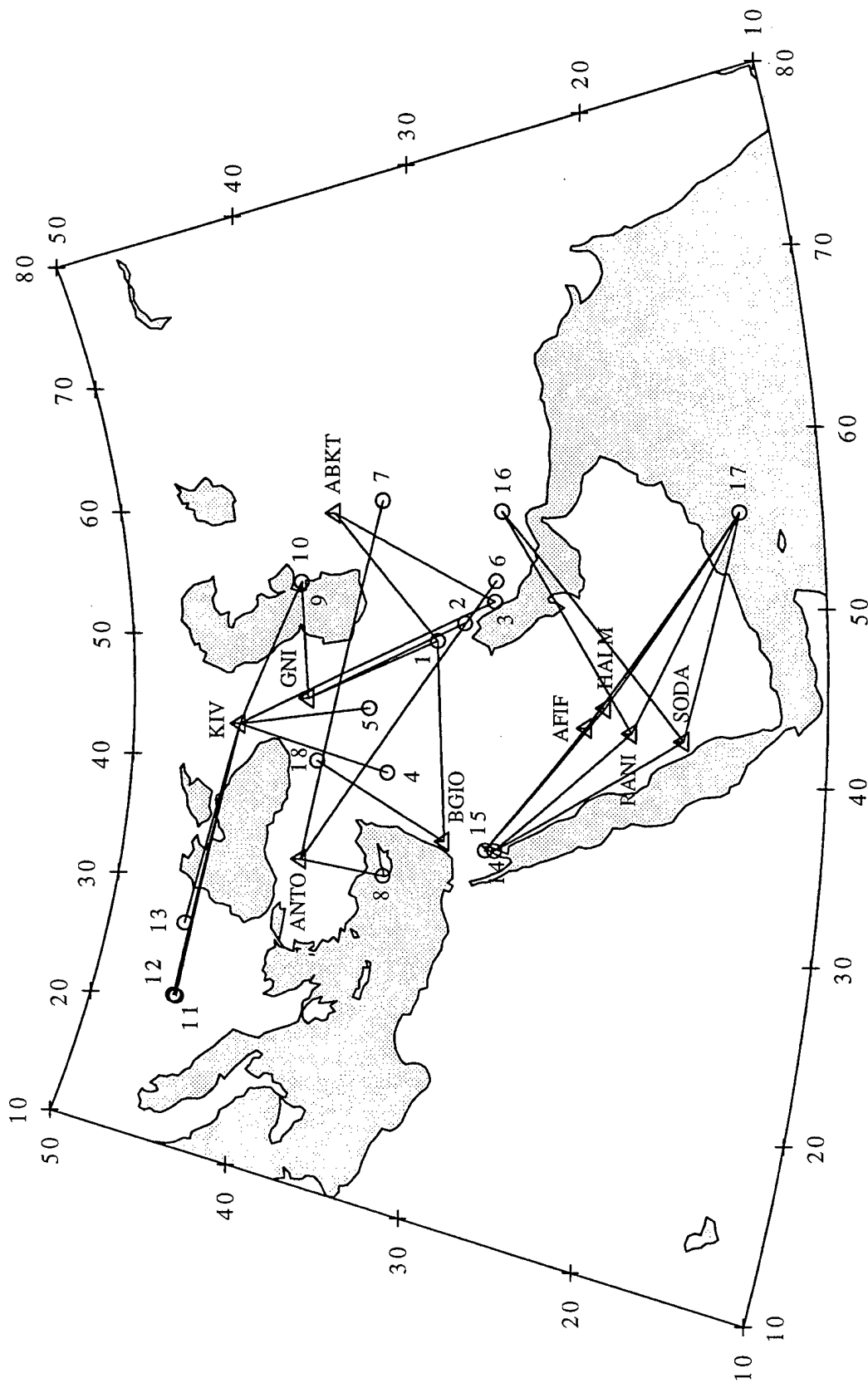


Figure 3

**Table 1.** Station Information

| Station | Latitude<br>(° N) | Longitude<br>(° E) |
|---------|-------------------|--------------------|
| ABKT    | 37.9304           | 58.1189            |
| ANTO    | 39.8689           | 32.7936            |
| BGIO    | 31.7220           | 35.0878            |
| GNI     | 40.0530           | 44.7240            |
| KIV     | 43.9562           | 42.6888            |
| AFIF    | 23.9310           | 43.0400            |
| HALM    | 22.8454           | 44.3173            |
| RANI    | 21.3116           | 42.7761            |
| SODA    | 18.2921           | 42.3769            |
| RAYN    | 23.5220           | 45.5008            |

the stations provided broadband digital data.

In the two-station method, 27 earthquakes were used as indicated in Table 2. The dates, origin times and locations of the earthquakes and recording stations are provided by the IRIS DMC. All but two of the earthquakes are less than 50 km in depth. The two exceptions (events 20 and 24 in Table 2) have depths of 75 and 62 km. In the study, all events lay within  $8^\circ$  in azimuth from great-circle paths between the two recording stations. The first station of each station pair in Table 2 is the closer of each pair to the epicenter. The rightmost column in Table 2 indicates the region that the surface waves traverse. Earthquakes 26 and 27 are not used for determinations of properties within any region since the waves from those events traverse three regions. They are only used to see if velocities and attenuations along those paths are consistent with our results for the individual regions.

18 earthquakes, listed in Table 3, were analyzed using the single-station method. All but one of the earthquakes (event 13 in Table 3) are less than 44 km in depth. The one exception has a focal depth of 88 km. For some events, records from several stations were available, whereas for some events only a single record was used because of the poor signal/noise ratios at other stations. Depths identified with an exclamation mark were determined by Harvard University and those identified with an asterisk were obtained in this study by matching the



**Table 2.** Earthquakes studied using the two-station method

| Event | Date   | Origin<br>(h:m:s) | Lat<br>(° N) | Lon<br>(° E) | Depth<br>(km) | Recording<br>stations | Az-dev 1<br>(°) | Az-dev 2<br>(°) | Region |
|-------|--------|-------------------|--------------|--------------|---------------|-----------------------|-----------------|-----------------|--------|
| 1     | 921006 | 08:57:17.7        | 38.42        | 56.52        | 10            | GNI-ANTO              | 3.6             | 1.9             | 1      |
| 2     | 941129 | 14:30:28.4        | 38.71        | 20.48        | 21            | ANTO-GNI              | 2.0             | 1.0             | 1      |
| 3     | 940329 | 07:56:53.9        | 29.10        | 51.26        | 33            | GNI-KIV               | 7.6             | 5.7             | 1      |
| 4     | 940920 | 05:51:46.0        | 32.50        | 48.77        | 33            | GNI-KIV               | 4.1             | 2.7             | 1      |
| 5     | 950422 | 00:21:48.6        | 30.89        | 49.91        | 25            | GNI-KIV               | 5.8             | 4.1             | 1      |
| 6     | 940524 | 02:05:36.2        | 38.66        | 26.54        | 17            | GNI-ABKT              | 7.1             | 4.1             | 2      |
| 7     | 940524 | 02:18:34.9        | 38.76        | 26.60        | 16            | GNI-ABKT              | 7.8             | 3.9             | 2      |
| 8     | 940603 | 22:40:21.2        | 28.74        | 70.07        | 33            | ABKT_KIV              | 6.9             | 3.6             | 2      |
| 9     | 931026 | 10:03:57.5        | 36.74        | 28.05        | 33            | ANTO-KIV              | 6.3             | 2.3             | 2      |
| 10    | 950103 | 22:51:45.0        | 34.94        | 23.55        | 33            | ANTO-KIV              | 1.3             | 0.7             | 2      |
| 11    | 950203 | 22:29:13.3        | 34.42        | 25.03        | 49            | ANTO-KIV              | 6.7             | 3.3             | 2      |
| 12    | 950330 | 18:17:15.1        | 34.40        | 24.79        | 7             | ANTO-KIV              | 5.8             | 2.9             | 2      |
| 13    | 960422 | 14:42:32.4        | 39.17        | 47.37        | 29            | AFIF-RANI             | 7.2             | 6.2             | 3      |
| 14    | 951123 | 18:07:17.3        | 29.33        | 34.75        | 10            | AFIF-HALM             | 4.7             | 4.0             | 3      |
| 15    | 951124 | 16:43:45.5        | 28.94        | 34.71        | 10            | AFIF-HALM             | 6.8             | 5.8             | 3      |
| 16    | 951125 | 11:41:35.3        | 29.12        | 34.84        | 10            | AFIF-HALM             | 5.5             | 4.7             | 3      |
| 17    | 951207 | 17:48:16.3        | 14.56        | 55.77        | 0             | HALM-AFIF             | 7.6             | 6.9             | 3      |
|       |        |                   |              |              |               | RAYN-BGIO             | 3.0             | 1.6             | 3      |
| 18    | 960328 | 07:28:28.1        | 11.92        | 57.81        | 10            | HALM-AFIF             | 4.9             | 4.5             | 3      |
| 19    | 960402 | 07:59:26.2        | 37.83        | 27.00        | 33            | AFIF-HALM             | 6.6             | 6.1             | 3      |
|       |        |                   |              |              |               | BGIO-HALM             | 4.6             | 1.8             | 3      |
| 20    | 960426 | 07:01:27.5        | 36.37        | 28.04        | 75            | AFIF-HALM             | 4.8             | 4.5             | 3      |
| 21    | 960225 | 16:14:10.9        | 35.65        | 57.07        | 33            | HALM-RANI             | 5.2             | 4.7             | 3      |
| 22    | 960225 | 17:42:04.5        | 35.65        | 57.05        | 33            | HALM-RANI             | 5.3             | 4.7             | 3      |
| 23    | 960331 | 16:02:09.3        | 31.83        | 49.03        | 0             | HALM-SODA             | 1.8             | 1.2             | 3      |
| 24    | 960103 | 08:42:26.3        | 39.03        | 48.72        | 62            | RANI-SODA             | 7.6             | 6.6             | 3      |
| 25    | 960128 | 08:43:16.2        | 34.26        | 46.45        | 33            | RANI-SODA             | 6.1             | 5.0             | 3      |
| 26    | 940610 | 03:00:44.5        | 38.56        | 70.63        | 33            | ABKT-BGIO             | 3.7             | 1.3             | 1,2,3  |
| 27    | 951026 | 04:23:27.5        | 39.18        | 72.07        | 50            | ABKT-BGIO             | 0.4             | 0.2             | 1,2,3  |

spectral holes of the theoretical spectra with those of the observed data. The dip, slip and strike angles were obtained by Harvard University. The number in the rightmost column of Table 3 indicates the region that the surface waves traverse.

## 5. Interstation Group and Phase Velocities

Before using the two-station method, we removed the mean ground motion from the records, corrected for geometrical spreading and instrument response, and applied bandpass filtering. Figure 4 is an example showing the original trace (top) recorded at station SODA for an earthquake that occurred on 28 January 1996, and the windowed trace of ground displacement (bottom) after correcting

**Table 3.** Earthquakes studied using the single-station method

| Event | Date   | Origin<br>(h:m:s) | Lat<br>(° N) | Lon<br>(° E) | Depth<br>(km) | Dip<br>(°) | Slip<br>(°) | Strike<br>(°) | Recording<br>stations   | Region |
|-------|--------|-------------------|--------------|--------------|---------------|------------|-------------|---------------|-------------------------|--------|
| 1     | 940920 | 05:51:46.0        | 32.50        | 48.77        | 15*           | 25         | 87          | 103           | ABKT, GNI<br>BGIO       | 1<br>3 |
| 2     | 950422 | 00:21:48.6        | 30.89        | 49.91        | 8*            | 32         | 72          | 117           | GNI                     | 1      |
| 3     | 940329 | 07:56:53.9        | 29.10        | 51.26        | 6*            | 40         | 104         | 334           | ABKT,KIV                | 1      |
| 4     | 941120 | 14:31:02.2        | 35.34        | 39.56        | 29            | 57         | 176         | 141           | KIV                     | 1      |
| 5     | 910724 | 09:45:41.8        | 36.52        | 44.07        | 10*           | 44         | 121         | 335           | KIV                     | 1      |
| 6     | 940620 | 09:09:02.9        | 28.97        | 52.61        | 14*           | 67         | -5          | 251           | ANTO                    | 1      |
| 7     | 941214 | 20:43:53.7        | 35.10        | 58.63        | 5*            | 32         | 144         | 319           | ANTO                    | 1      |
| 8     | 950223 | 21:03:01.3        | 35.05        | 32.28        | 15!           | 21         | 140         | 239           | ANTO                    | 1      |
| 9     | 940701 | 10:12:41.2        | 40.23        | 53.38        | 44!           | 30         | 71          | 251           | GNI,KIV                 | 2      |
| 10    | 940701 | 19:50:04.3        | 40.22        | 53.39        | 44            | 34         | 108         | 290           | GNI,KIV                 | 2      |
| 11    | 910712 | 10:42:21.2        | 45.36        | 21.06        | 11            | 78         | -1          | 279           | KIV                     | 2      |
| 12    | 911202 | 08:49:40.2        | 45.50        | 21.12        | 9             | 72         | -5          | 103           | KIV                     | 2      |
| 13    | 900531 | 00:17:47.8        | 45.81        | 26.77        | 88            | 26         | 54          | 90            | KIV                     | 2      |
| 14    | 960221 | 04:59:51.2        | 28.80        | 34.78        | 10            | 30         | -104        | 132           | RANI,SODA               | 3      |
| 15    | 951123 | 18:07:17.2        | 29.33        | 34.75        | 26*           | 77         | 7           | 199           | AFIF,HALM               | 3      |
| 16    | 960226 | 08:08:19.2        | 28.32        | 57.09        | 33            | 7          | 125         | 315           | RANI,SODA               | 3      |
| 17    | 960314 | 21:47:57.9        | 14.74        | 55.74        | 18*           | 20         | -118        | 72            | AFIF,RANI,<br>HALM,SODA | 3      |
| 18    | 951205 | 18:49:30.4        | 39.44        | 40.15        | 29!           | 70         | 160         | 136           | BGIO                    | 1,3    |

for geometrical spreading and instrument response, and bandpass filtering between corner frequencies of 0.01 and 1 Hz. The epicentral distance and the starting times of the traces from the origin are indicated in the boxes. The dashed lines above the top trace represent the window with a 10% cosine taper. In this example, the window length is 400 sec, and the starting and ending times correspond to group velocities of about 2.2 to 4.5 km/sec, respectively.

The Multiple Filter Technique (MFT) was then utilized to extract group velocities. Figure 5 shows contoured spectral amplitudes of fundamental- and higher-mode Rayleigh waves obtained for an earthquake that occurred on 22 April 1995 and recorded at station GNI. The windowed ground displacement, after correction for the geometrical spreading and instrument response, and bandpass filtering, is displayed at the rightmost part of the figure. The same trace with a linear group velocity scale is plotted adjacent to the dispersion diagram. This trace can be used to correlate group velocity contour values to the

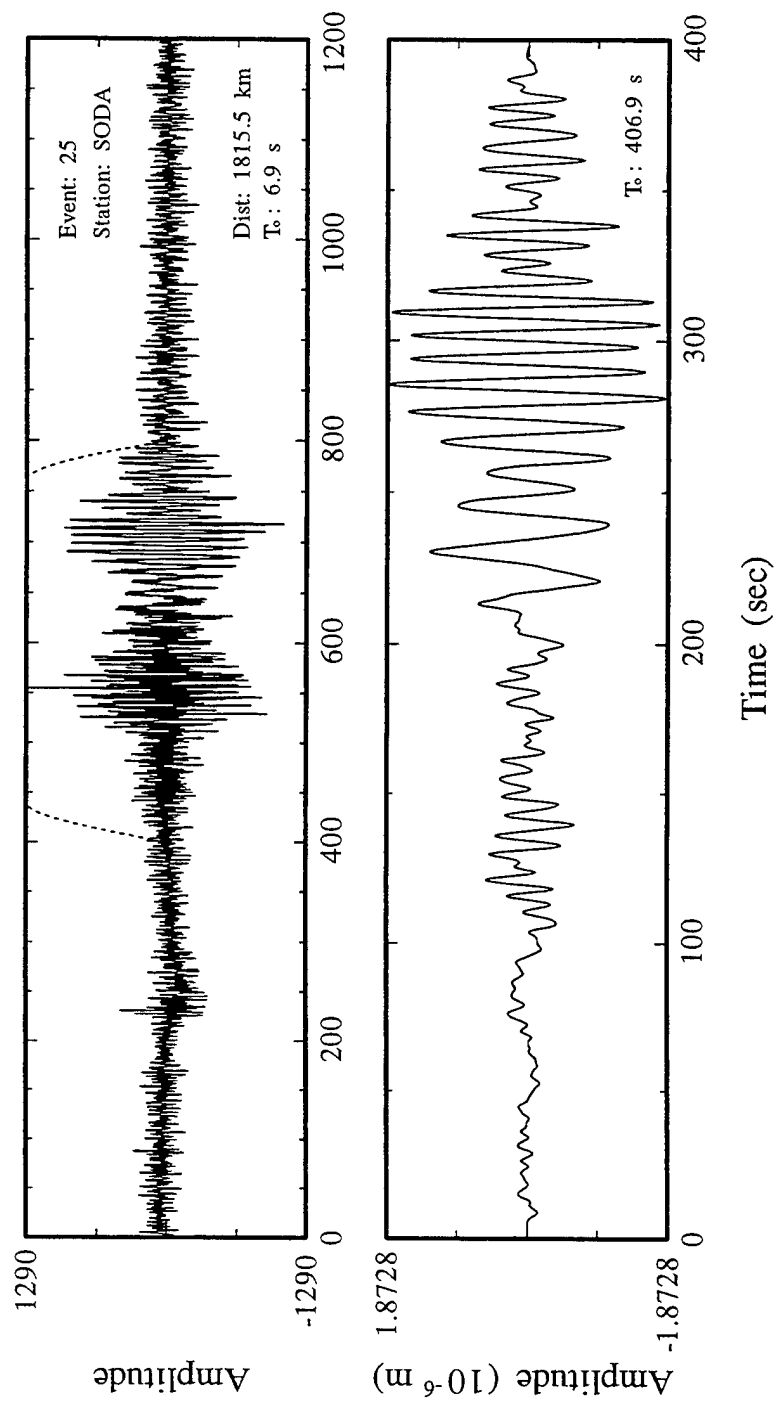


Figure 4

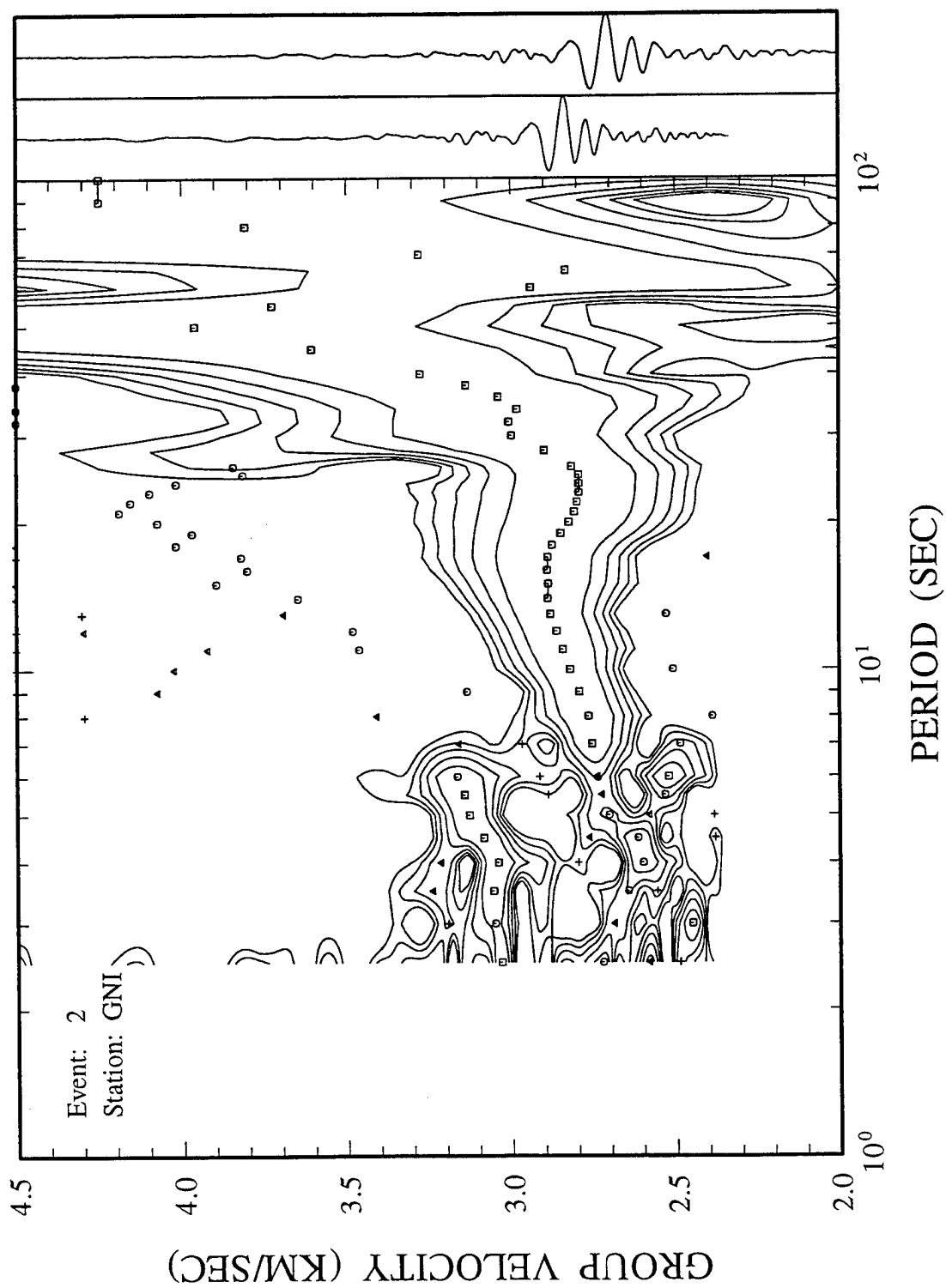


Figure 5

trace itself. The long, smooth curve composed of squares identifies the fundamental-mode group velocity dispersion. The shorter curve with a group velocity of about 3.1 km/s at 5 sec is a superposition of higher modes. The square, circle, triangle, and plus signs correspond to the four largest amplitudes in the time domain when the MFT is applied.

A phase-matched filter technique as proposed by Herrin and Goforth (1977), and coded by Herrmann (1987) was used to extract the phase-velocity information. The interstation group and phase velocities can then be obtained for the three regions as shown in Figures 6, 7, and 8. In each of the three figures, group velocities appear below the phase velocities.

Different features can be observed for the dispersion curves of the three regions. For Region 1 (Figure 6), the group velocities obtained for different events are similar to one another at periods below 20 sec and display greater scatter at longer periods. The velocities increase rapidly with increasing period at shorter periods, and reach a value of about 2.89 km/s at 10 sec. The velocity values remain almost unchanged in the period range 10-20 sec. Above 20 sec, the velocities increase again, smoothly and monotonically, reaching their maximum values at the maximum observable period. The phase velocity curves for this region, however, increase uniformly throughout the entire period range.

Most of the curves for Region 2 (Figure 7) are similar to one another, but velocities in a few cases deviate substantially from mean values. This deviation may be due to systematic errors caused by lateral variations of properties in this region. It is comprised of both oceanic (Black and Caspian Seas) and continental portions. Both phase and group velocities, at shorter periods, are lower than those for Region 1. This implies that the shear velocities at shallow depths in Region 2 are lower than those in Region 1.

Fifteen interstation group and phase velocities are obtained for Region 3 (Figure 8). The largest interstation distance is 1370 km between stations BGIO and RAYN. The distances for the station pairs AFIF-RANI, AFIF-HALM, HALM-

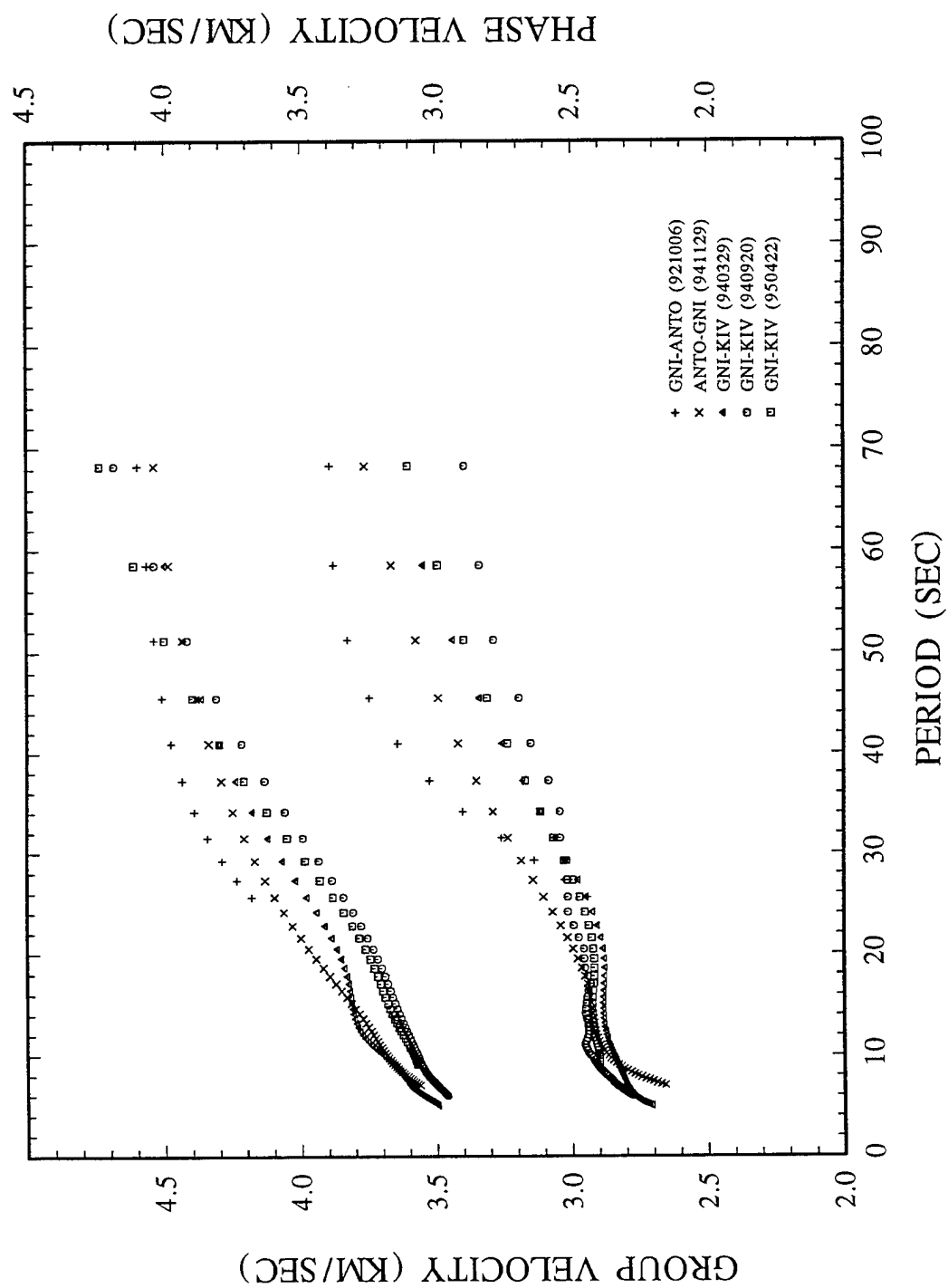


Figure 6

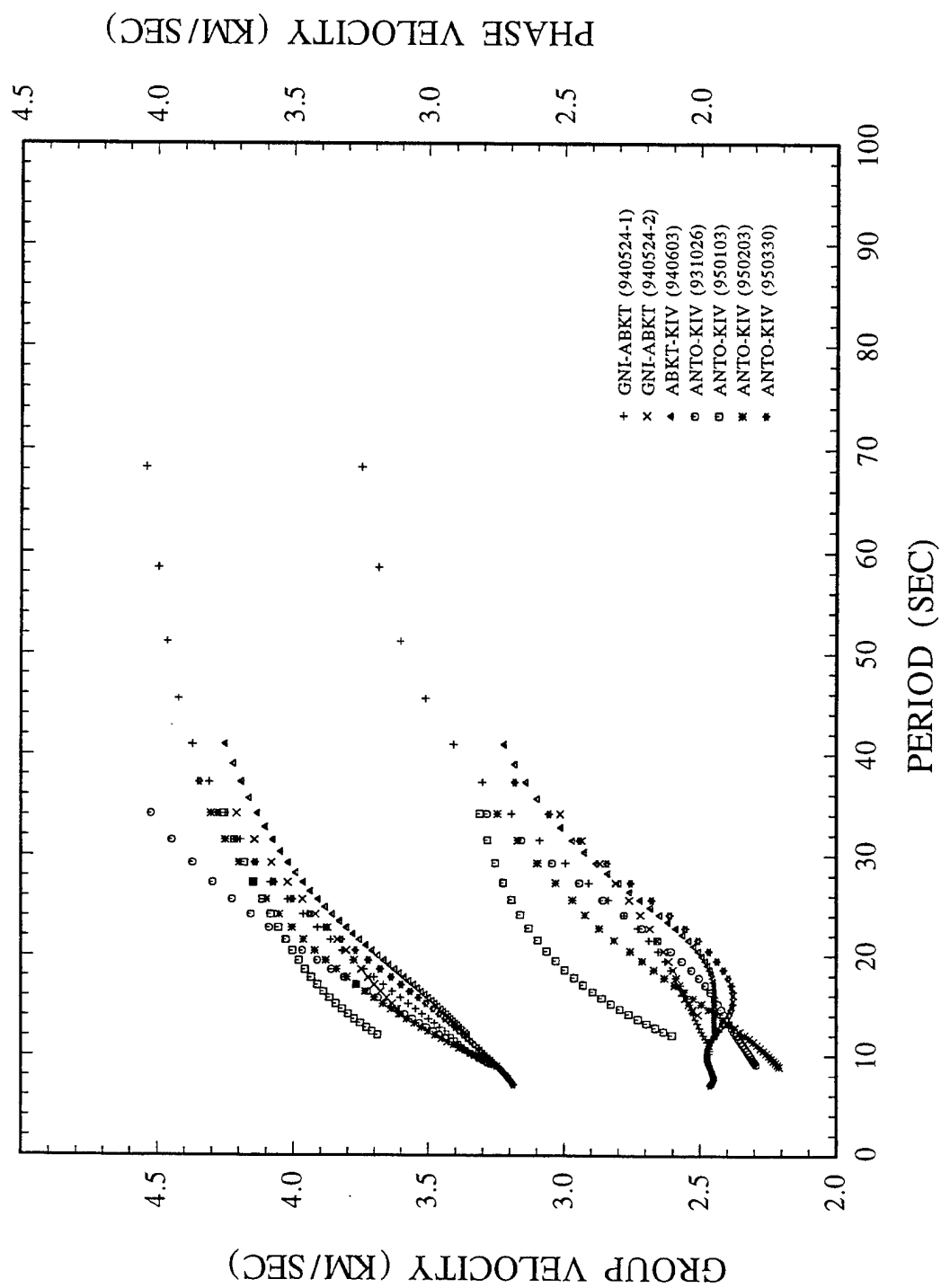


Figure 7

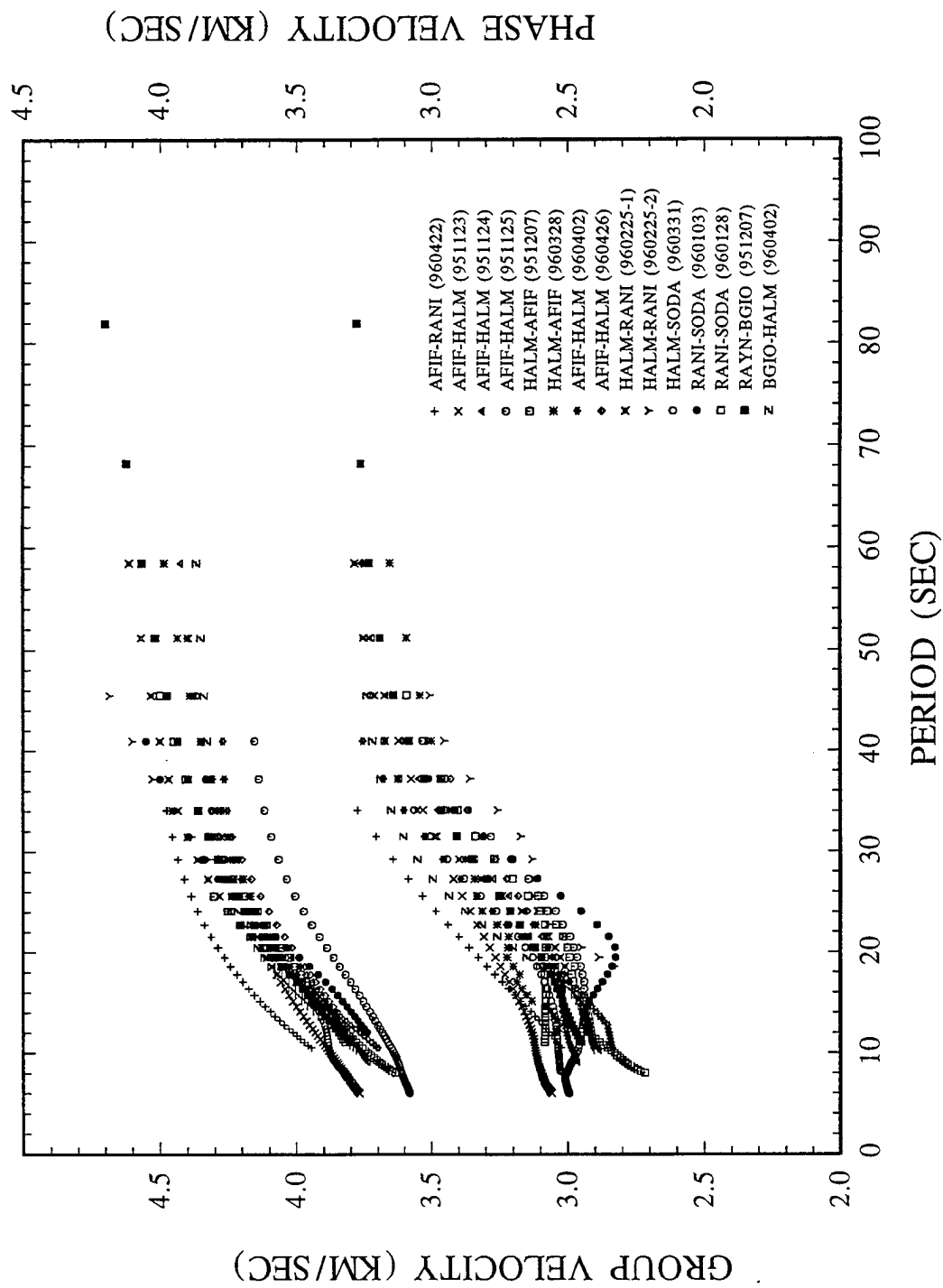


Figure 8



RANI, and HALM-SODA are, however, in the range 178-543 km. Short interstation distances can cause problems when using the two-station method. Any departures from a great-circle path or measurement errors can result in severe bias in the velocity and attenuation determinations. To control the errors, we tried to collect as many events for each station pair as possible. For example, seven events were used for the station pair AFIF-HALM. If observed values are similar, the standard deviations of the mean values will be reduced. In addition, results for the station pairs with shorter interstation distances will be compared with those with longer interstation distances, and also be compared with the average values to examine the usability of the data. The curves for the station pairs RAYN-BGIO and BGIO-HALM lie in the middle of the group, suggesting that the selected curves for the shorter interstation distances are realistic. The models obtained after inversion will be compared with those reported in the previous studies to check the validity of the interstation results. The mean value of group velocities at 10 sec for Region 3 is higher than that found for either Region 1 or 2, being about 2.98 km/s. This suggests that the near-surface shear velocity is higher here than in the other two regions.

The interstation group and phase velocities for the station pair ABKT-BGIO are plotted in Figure 9. The paths connecting the two stations cross the southern edge of the Caspian Sea, the Turkish and Iranian Plateaus, and the northern Arabian Peninsula as shown in Figure 2. According to our regionalization, the paths cross all of the three regions. Since our goal is to obtain velocity and attenuation structure for individual regions, we did not use the dispersion data for this station pair in our inversion. If our regionalization is appropriate, i.e. the three regions are geologically different with different velocity and attenuation structure, the group and phase velocities, and the attenuation values for this station pair should give an average for the three regions. The average group velocities at 10 sec are about 2.89, 2.35, and 2.98 km/s for Regions 1, 2, and 3, respectively. The average group velocity at 10 sec for these two events is about 2.70 km/s,

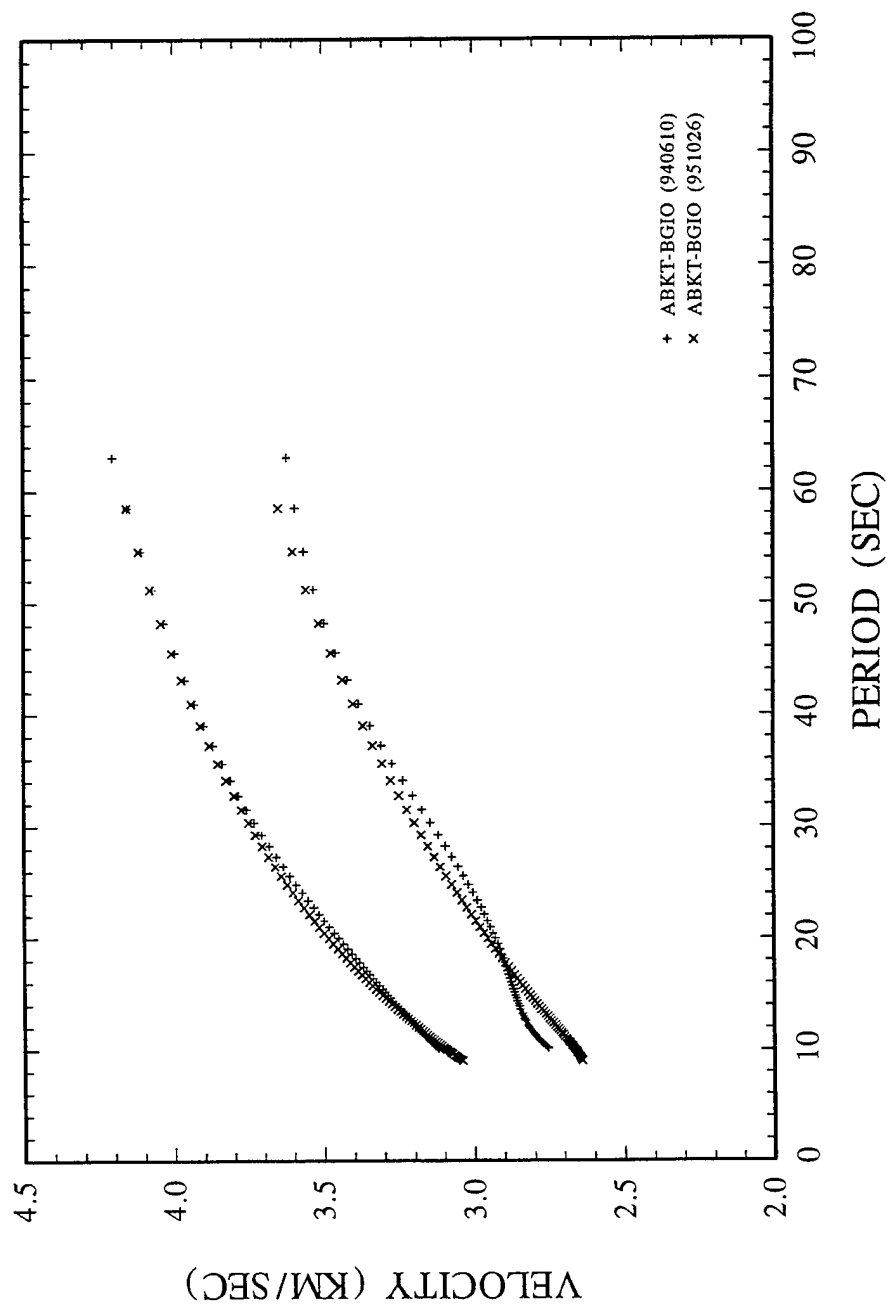


Figure 9

which is in the middle of the three values. The velocities increase with period and have a value of about 3.38 km/s at 40 sec, which is also in the middle of the average values of 3.33, 3.30, and 3.55 km/s for Regions 1, 2, and 3 at that period, respectively. The group velocities for these two events are higher than those for Region 2, lower than those for Region 3, and similar to those for Region 1 for the periods greater than 20 sec. The average phase velocity for these two events at 10 sec is about 3.12 km/s. This value is also in the middle of the corresponding values, 3.13, 2.82, and 3.28 for the three regions. From the above comparisons, we conclude that our division of the Middle East into three regions is appropriate.

## **6. Shear Velocity Models Obtained Using the Two-station Method**

Since the dispersion curves in each group exhibit similar features, the average values and the standard errors were calculated for each of the three regions. It should be noted, however, that for some periods only single observations are available and the standard deviations cannot be calculated. In these cases, we compared the measurement errors at these periods with the estimated standard deviations at other periods where multiple observations are available, choosing the largest values as our conservative error estimates. We chose 0.3 km/s as the error estimates at those points.

To save computing time, the average dispersion data were simplified to make a roughly even distribution over a linear period range. The simplified group and phase velocities were then inverted using a differential inverse technique to obtain the shear-velocity models for the three regions. In the inversion process, the thickness of each layer was fixed. The initial values of compressional and shear velocities, and densities are 6.0 km/s, 3.5 km/s, and 3.0 g/cm<sup>3</sup> for all of the layers. These values were changed later to see the effect of initial values on inversion results. Figure 10 is an example showing the shear velocity models and the resolving kernels obtained by inverting the fundamental-mode Rayleigh data for Region 1. The left panel of the figure shows the velocity model, whereas the

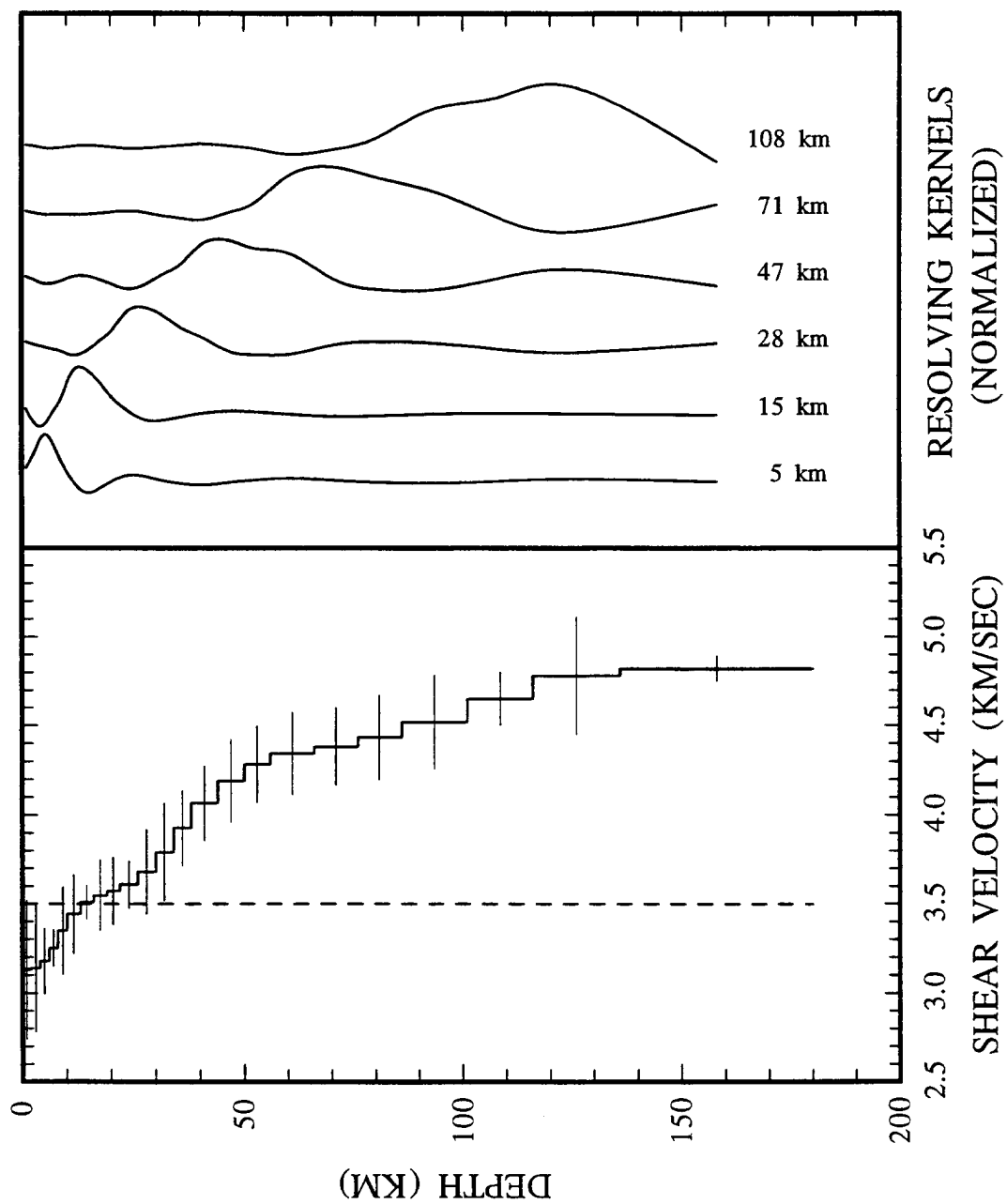


Figure 10

right panel gives the normalized resolving kernels at six depths. The dashed line in each figure represents the initial value of the shear velocities, 3.5 km/sec. The lateral bars are the error estimates of the corresponding velocity values, plotted at the midpoint of the corresponding layers. Figure 11 shows the observed group and phase velocities as well as the theoretical dispersion curves predicted by the model obtained for Region 1. The circles denote the group velocities, whereas the squares represent the phase velocities. The vertical bars are the standard errors of the data. The curves for the resolving kernels on the right panel of Figure 10 show that the shallow structure is better resolved than the deeper structure. The shapes of the velocity resolving kernels are similar for all of the three regions, and are therefore not plotted for the other two regions. The velocity models obtained in this study, from analysis of the resolving kernels, are restricted to the crust and the uppermost part of mantle within a depth of about 120 km. The match of the theoretical velocity dispersion curves to the observed data (Figure 11) is good over the entire period range. Similar results were obtained for the other two regions, and are not plotted. For comparison, we plot the shear-velocity models for the three regions together in Figure 12. The dotted, dashed, and solid lines are the models for Regions 1, 2, and 3, respectively. The uncertainties of the velocities in each layer are also plotted as horizontal bars, which overlap for the deeper layers. The velocities for the three regions differ greatly in the upper 10 km. Region 3 has the highest velocity values, whereas Region 2 has the lowest velocities. The average velocities for the upper 10 km are about 3.21, 2.85, and 3.39 km/s for Regions 1, 2, and 3, respectively. Below 10 km in the crust, the velocities in Regions 2 and 3 increase gradationally without any obvious gradient change, whereas the velocity gradient in Region 1 changes significantly at depths between about 12 and 30 km. In the uppermost mantle, the velocity gradients decrease for all of the three regions, and velocity values in the uppermost mantle do not differ much from region to region, especially for Regions 1 and 3. At depths near 120 km the velocities for the three regions approach a high value in the

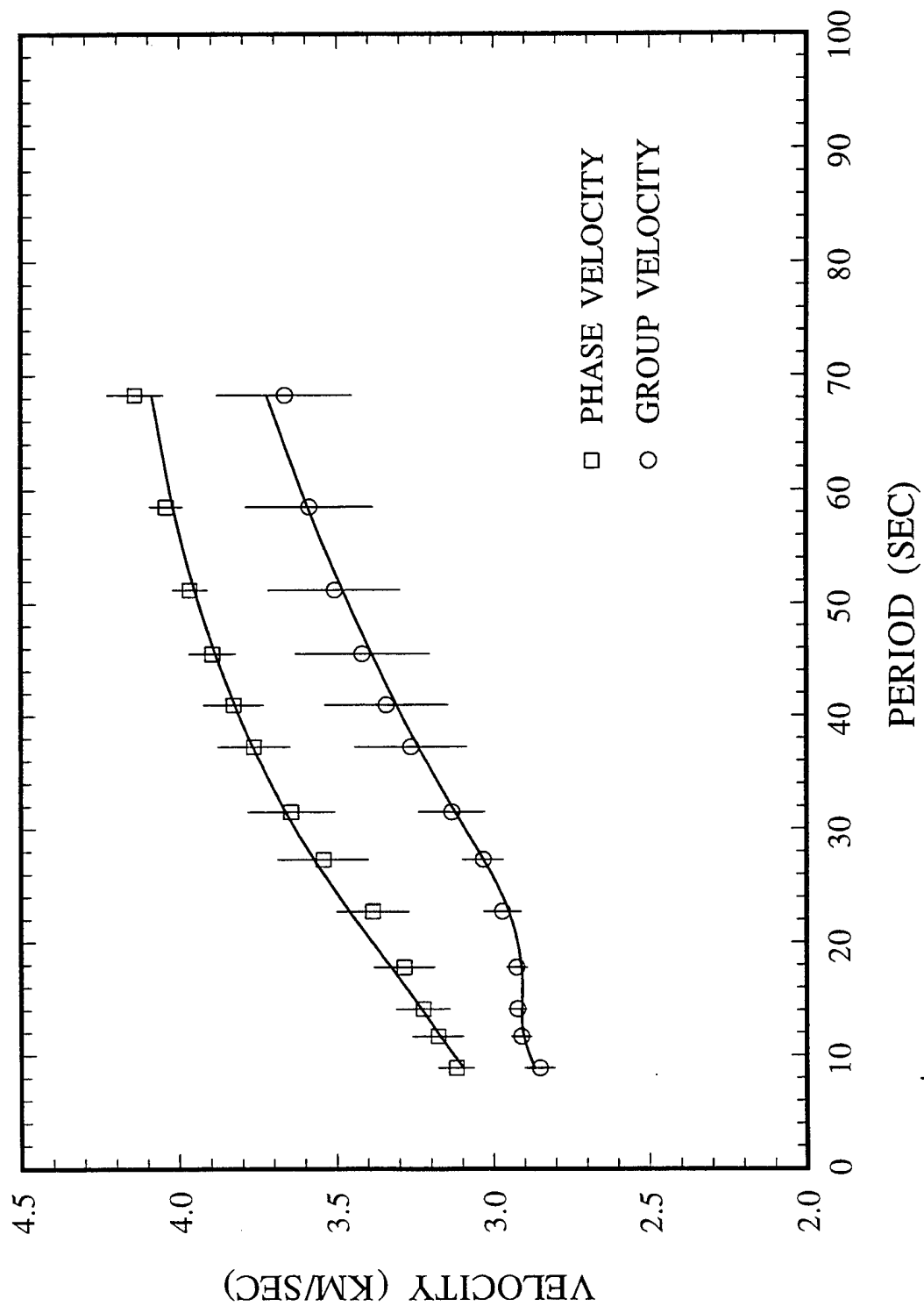


Figure 11

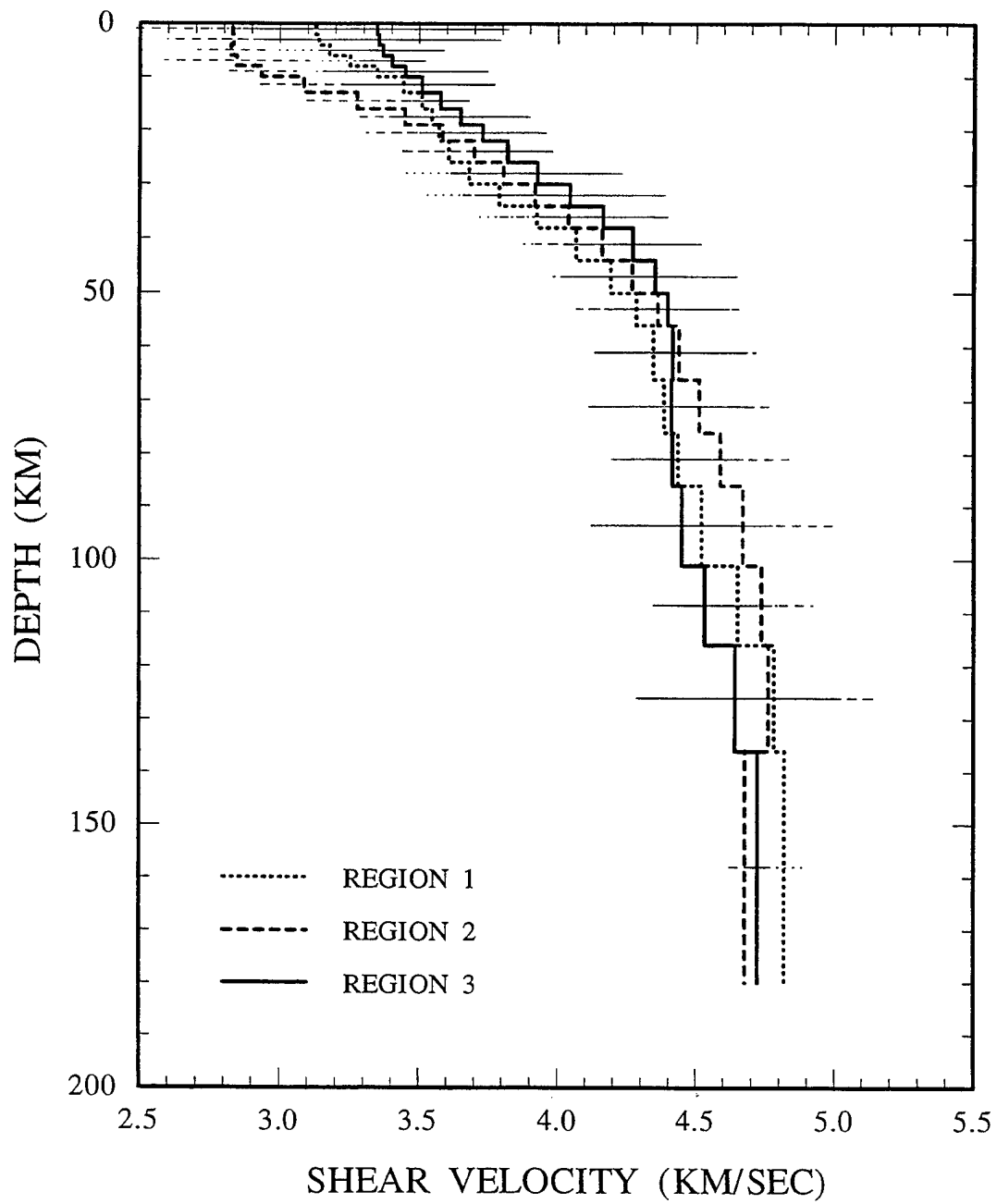


Figure 12

range 4.64-4.78 km/s. No low-velocity zones are resolved for any of the three regions in the present study. Since Region 2 includes both continental and oceanic portions, the model for this region may not represent either of those portions very well.

Figure 13 compares our velocity models with those of other studies in the Arabian Peninsula. The bold line is the model obtained in this study, whereas the thin lines and dashed or dotted lines represent the results from other studies. The models labeled by "Crust H" and "Crust L" are cited from the study of Knopoff and Fouda (1975). Their study showed a variety of solutions which can explain the data. We selected two typical models, in the depth range 0-180 km, from the Crust H and Crust L models to compare with our model.

Mokhtar and Al-Saeed (1994), using data recorded by station RYD in the center of Arabian Peninsula, studied three major propagation paths. Path I connects the station and the events in the Red Sea, Path II is for the events in Gulf of Aden, and Path III is for the events in the Zagros folded zone. The results are plotted in Figure 13 using the lines labeled by Path I, Path II, and Path III, respectively. Because the period range of the dispersion data is from 4 to 42 sec, the maximum depth for the models is 60 km.

Ghalib (1992) used data recorded at several stations surrounding the Arabian Peninsula to invert for the velocity structure using a single-station method. Since his maximum period is about 70 sec, the maximum depth he used for the inversion is 100 km. Many paths were included in his study. For purposes of comparison, we select only two typical paths crossing the entire Arabian Peninsula, one trending north-south, another trending east-west. The models for the two paths are plotted in Figure 13 as the lines labeled by T190 and S212f.

Figure 13 shows that the shear-velocity model obtained in this study is in good agreement with models obtained in other studies, especially for the depth range 20-40 km. For the upper 20 km, our velocities agree with the average of other studies because we used paths at several azimuths, and averaged the



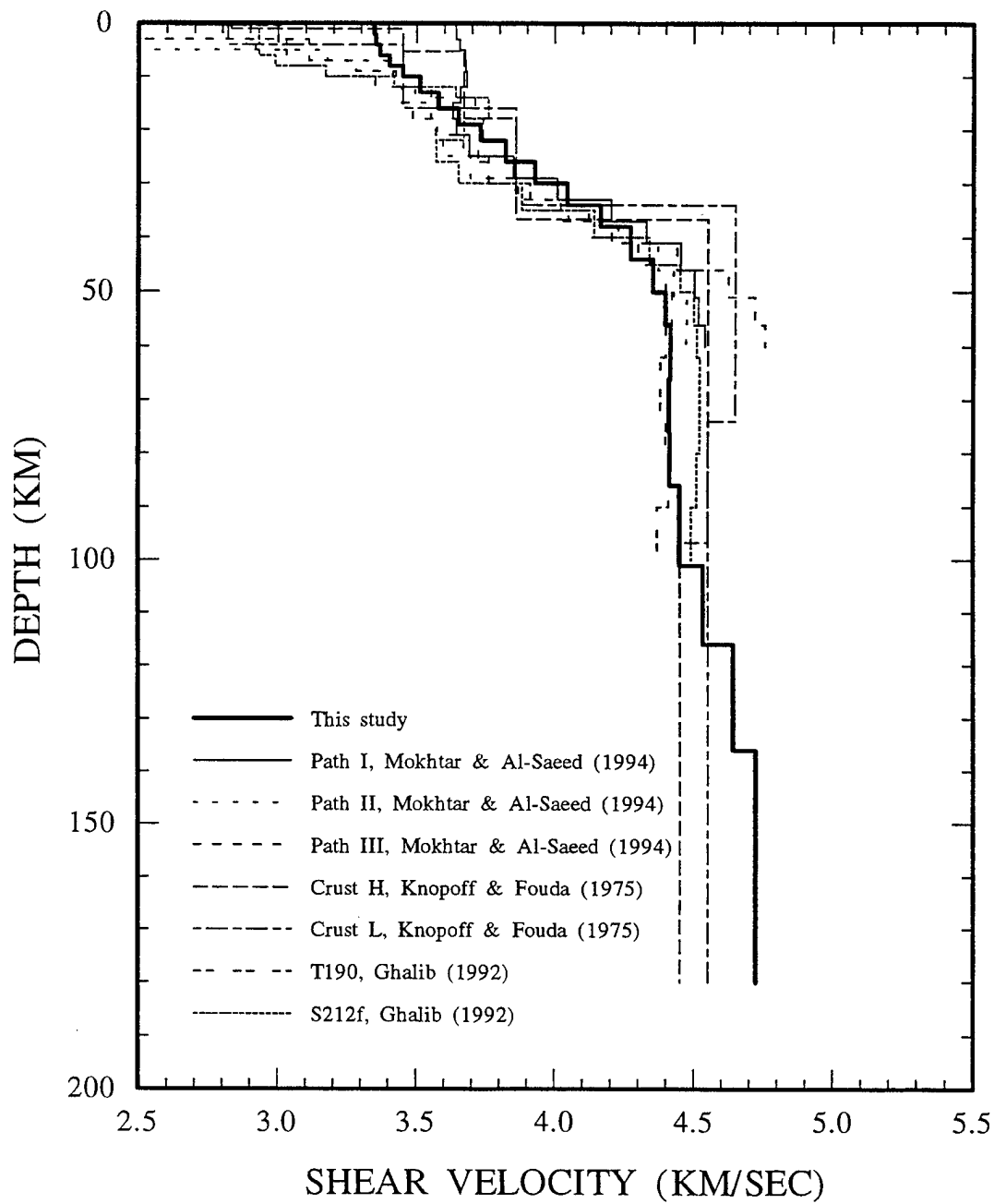


Figure 13

dispersion values to obtain an average velocity model for the entire peninsula. For the uppermost mantle, at the depths 40-100 km, there is a wide range of velocities (4.4-4.7 km/s). The model obtained in this study (4.4 km/s) lies in the lower portion of that region.

The velocity model of Region 1 is compared with those of Mindevalli and Mitchell (1989) as shown in Figure 14. In their study, the region is divided into two subregions: eastern and western Turkey. The figure shows that the velocity model of this study is in good agreement with their models. In the lower crust and the uppermost mantle (20-80 km) the three models are nearly identical. For the upper crust, the model of this study agrees well with the model for eastern Turkey, and is slightly higher than that for western Turkey. This is not surprising because the path connecting stations ANTO and GNI is located within eastern Turkey. In addition to using data for the station pair ANTO-GNI, we have used data from the station pair GNI-KIV to determine an average velocity model for this region. The model, therefore, appears to be valid for the mountain area between the Black Sea and Caspian Sea as well as for eastern Turkey.

In the inversion process, we used an initial velocity value of 3.5 km/s for all layers. The velocity models obtained can be affected by the initial model values, especially at depths where the resolving kernels are broad. To investigate the effect of initial values on the inversion results, we performed the inversion two more times, using initial values of 4.0 and 4.5 km/s separately for all layers. The predicted group and phase velocities, and the resolving kernels are almost identical to those previously obtained. They are, therefore, not plotted here. The velocity models obtained using different initial values for the three regions are presented in Figure 15. The bold, thin, and dashed lines in each set of curves correspond to the initial values of 3.5, 4.0, and 4.5 km/s, respectively.

Figure 15 indicates that the velocities at crustal depths are not changed by the variation of the initial values. At mantle depths the changes in velocity are very limited, far less than the error estimates. None of the curves approaches the

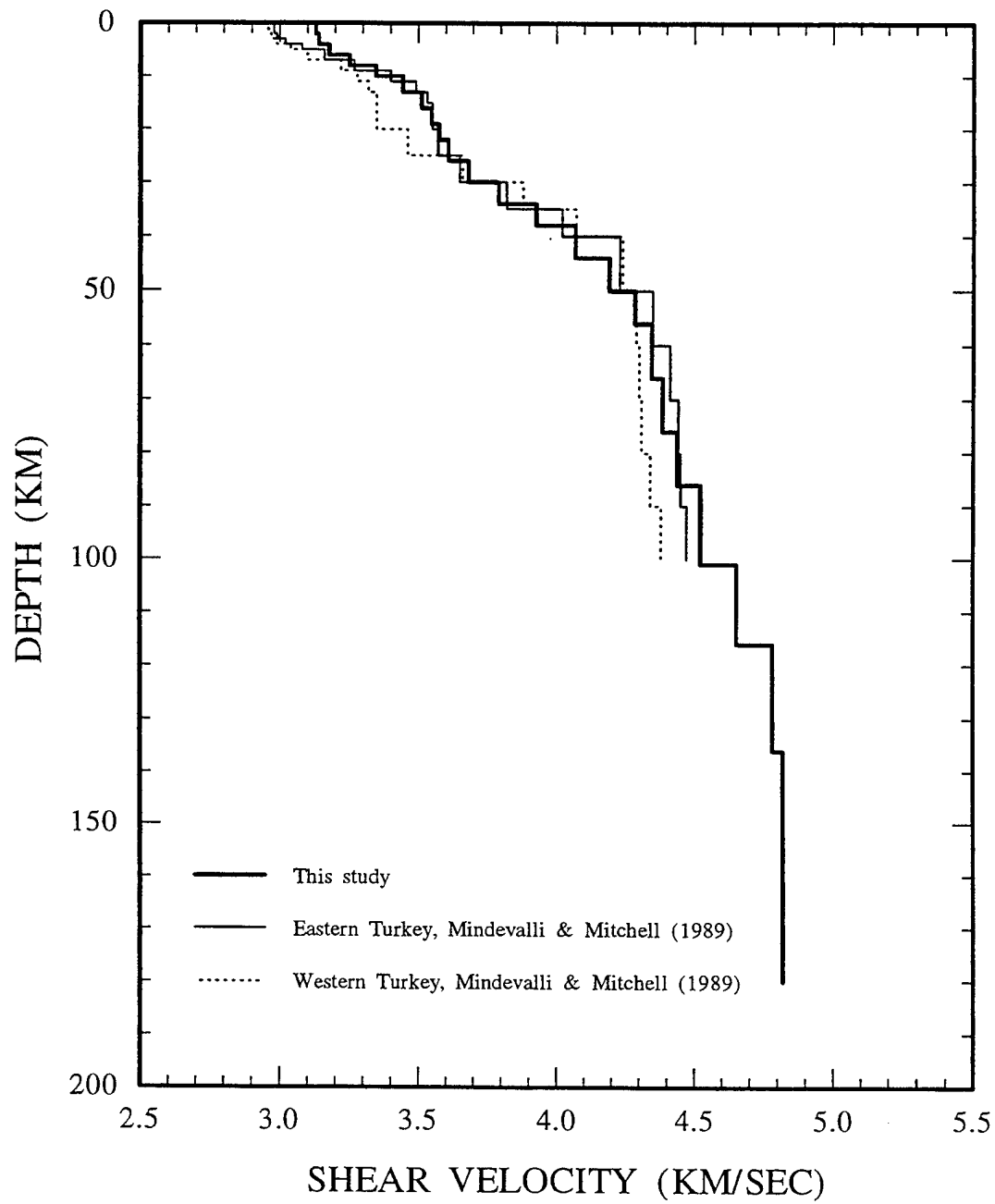


Figure 14

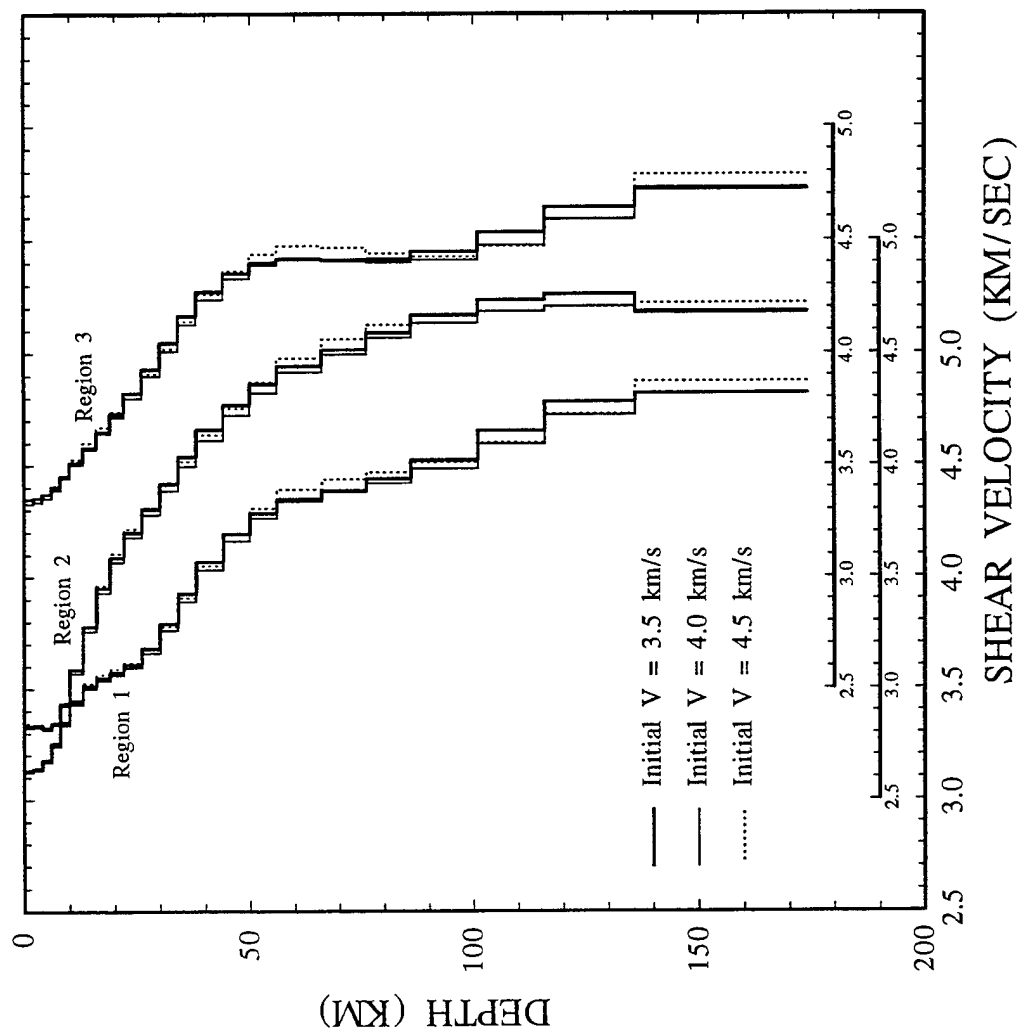


Figure 15

initial values at great depths. We conclude that the models for the three regions are not affected by the initial values throughout the depth range. Conservatively speaking, the velocities can be resolved to at least 120 km, a depth similar to that suggested by the resolving kernels.

## 7. Shear-wave $Q$ Models Obtained Using the Two-station Method

Figure 16 shows the interstation attenuation coefficients ( $\gamma$ ) for Region 3. As with velocities, we calculated the average value of  $\gamma$  for each of the three regions. For the periods where only a single measurement is available, a value of  $0.5 \times 10^{-3} \text{ km}^{-1}$  was chosen as a conservative error estimate. The average attenuation data were then simplified to make a roughly even distribution over a linear period range. The differential inverse procedure was used to obtain the  $Q_\mu$  models for the three regions, taking 0.0 as an initial value of  $Q^{-1}$  for all layers. Figure 17 is an example showing the  $Q_\mu$  models and the resolving kernels for Region 3. The final  $Q_\mu$  model with standard deviations is plotted along with the starting model in the left panel. The right panel gives the normalized resolving kernels at six depths. The resolving kernels for  $Q_\mu$  are similar for all of the three regions, and those for the other two regions are, therefore, not plotted.

Figure 17 shows that the resolving kernels for  $Q_\mu$  are wider at great depths than those for the shear velocity. This indicates that the applicable depth of our  $Q_\mu$  models are shallower than that of shear velocity. We restrict the  $Q_\mu$  models of this study to the uppermost 80 km. The observed attenuation coefficients and theoretical dispersion curves predicted by the model for Region 3 are plotted in Figure 18. The agreement between them is good over the entire period range. Similar results were obtained for the other two regions, and are not plotted. The  $Q_\mu$  models obtained for the three regions are presented in Figure 19. The dotted, dashed, and solid lines are the models for Regions 1, 2, and 3, respectively. The uncertainties in  $Q_\mu$  values for each layer are also plotted as horizontal bars, which overlap for deeper layers. The  $Q_\mu$  models show different features from

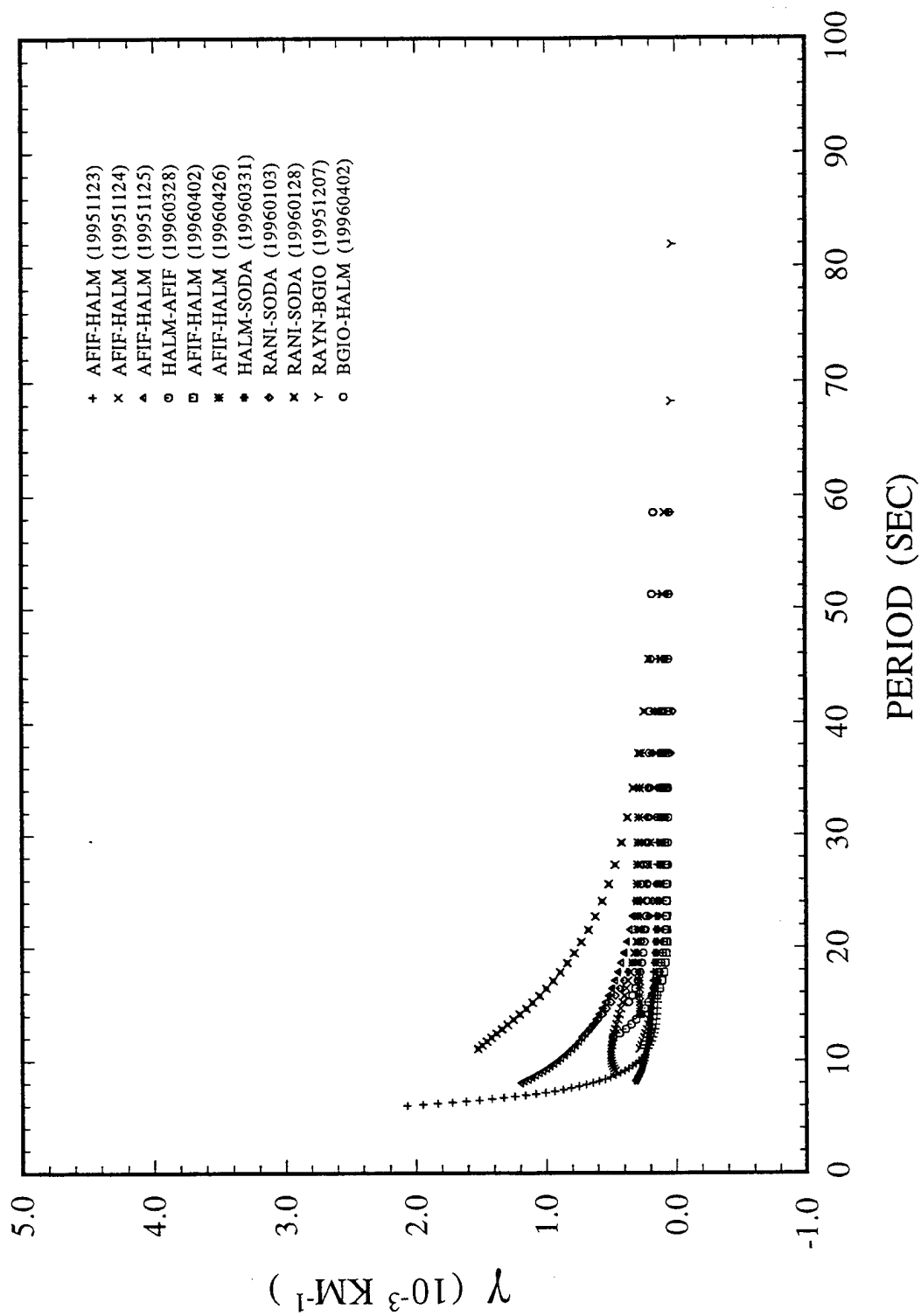


Figure 16

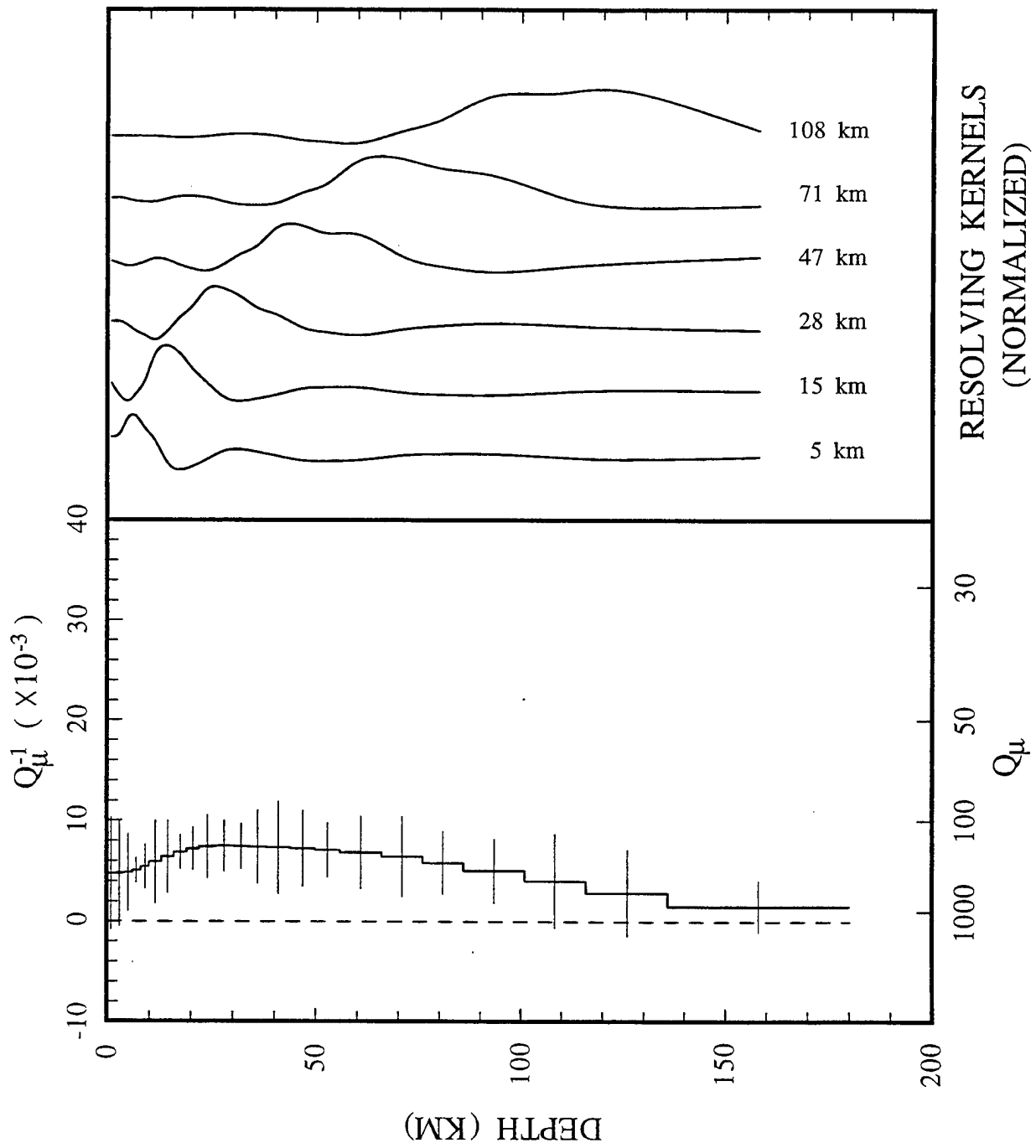


Figure 17

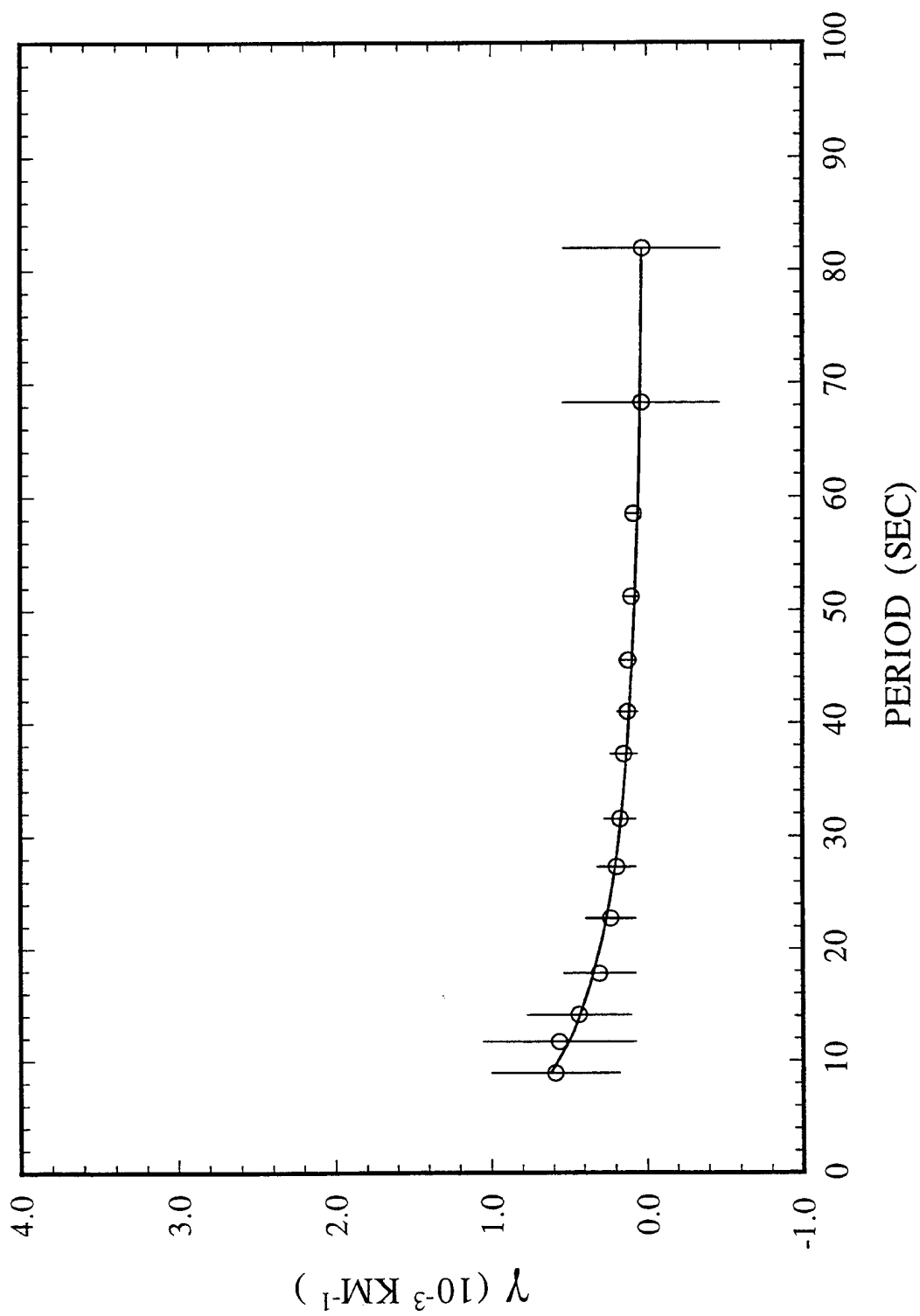


Figure 18



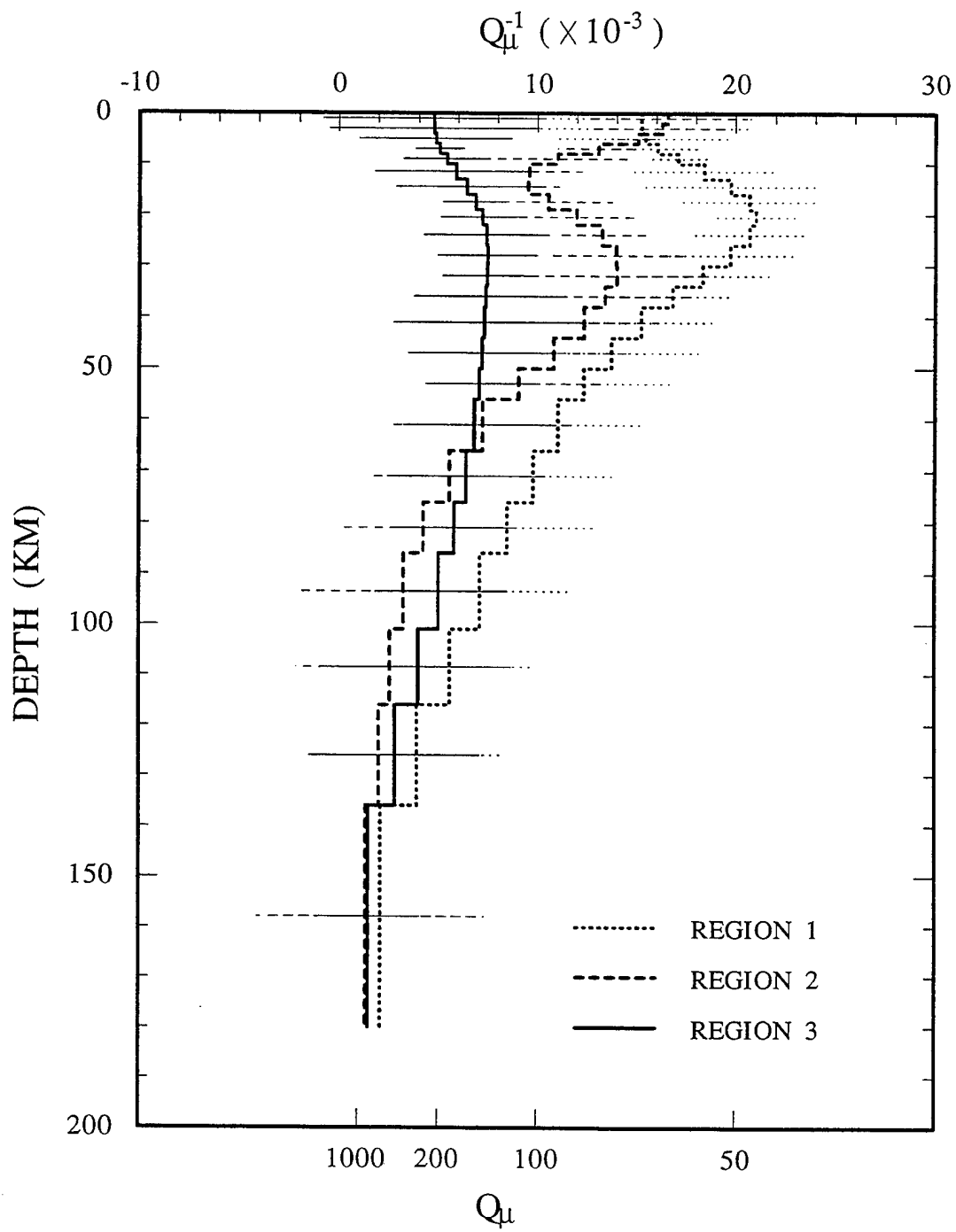


Figure 19

region to region.  $Q_\mu$  in Region 3 is highest through the upper 60 km, whereas  $Q_\mu$  in Region 1 is the lowest in the same depth range. For the upper 10 km, the average  $Q_\mu$  values for Regions 1, 2, and 3 are 63, 71, and 201, respectively.  $Q_\mu$  values for Regions 1 and 3 decrease with depth in the upper crust, whereas  $Q_\mu$  for Region 2 increases. The  $Q_\mu$  model for Region 1 has a minimum at a depth of 20 km. The  $Q_\mu$  model for Region 3 exhibits a zone of constant  $Q$  in the depth range 20-80 km. The  $Q_\mu$  model for Region 2 fluctuates, having a minimum and a maximum at depths of about 12 and 30 km, respectively. This feature may be specious, and is probably due to systematic errors in our one-dimensional inversion in a region where  $Q_\mu$  varies rapidly in three dimensions. As with the discussion for velocities, we think that details of the  $Q_\mu$  model for this region should be ignored. At depths greater than 80 km, the  $Q_\mu$  values for all three regions increase gradually, approaching the initial value.

We originally used a initial value of 0.0 for  $Q_\mu^{-1}$  in the inversion. We tested the effect of initial values of  $Q_\mu$  on the resulting  $Q_\mu$  models by inverting using initial values of 0.005 and 0.01 to  $Q_\mu^{-1}$  (corresponding to  $Q_\mu$  values of 200 and 100). The resulting models for the three regions are presented in Figure 20. The  $Q_\mu$  models are more easily affected by the initial values than are the velocity models, indicating that the resolvable depth is less than that for the velocity. At crustal depths, none of the models for the three regions is greatly affected by the variation of initial values, indicating that resolution is good at those depths. The depths at which the three curves corresponding to the three initial values begin to deviate are about 80, 120, and 90, for Regions 1, 2, and 3, respectively. At greater depths, the  $Q_\mu$  values approach the initial values, indicating poor resolution at those depths. To be conservative, we choose 80 km as the applicable depth of the  $Q_\mu$  models for all three regions. All of our conclusions concerning the  $Q_\mu$  models will be restricted to this depth. This is also in agreement with the result obtained by analysis of the resolving kernels. Our results indicate that the resolvable depth for  $Q_\mu$ , when inverting Rayleigh wave data, is less than that for

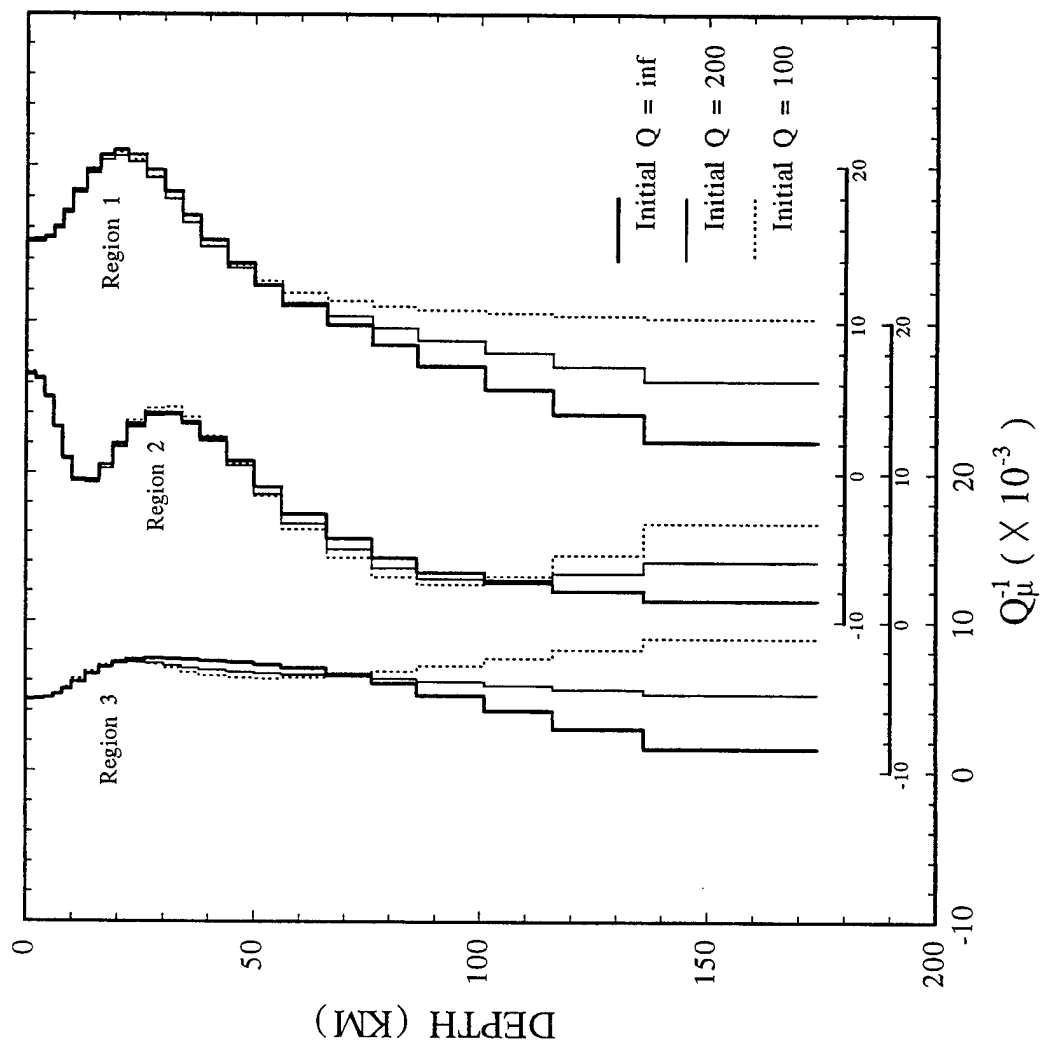


Figure 20

shear velocity.

## 8. Shear-wave $Q$ Models Obtained Using the Single-station Method

Determination of surface wave attenuation, using the two-station method, requires that the azimuths between earthquakes and stations are similar to the azimuths of the line connecting the two stations. This greatly reduces the number of usable earthquakes. In addition, if the two stations are located in different geological provinces, only the average attenuation of the different provinces between the two stations can be obtained. For these reasons, a single-station method was developed by Cheng and Mitchell (1981) for the purpose of improved regional attenuation studies. The importance of the method lies in its ability to utilize relatively short paths between a single source and a single receiver, both of which are preferably located within a single geological province.

The method attempts to match theoretical and observed surface wave spectra. This is done by a trial-and-error procedure in this study. The method utilizes both fundamental-mode and higher-mode spectra since use of the amplitude ratios for the two spectra obviates the need to know the seismic moment of the earthquake used. To extract the observed spectrum, the multiple-filter technique was applied to the data as described in the previous section. Computations of theoretical surface-wave spectra requires knowledge of the source mechanism of the earthquake. For all of the earthquakes we used the focal mechanism determined by Harvard University.

Figure 21 is an example showing the process of  $Q_\mu$  determination for each layer. The earthquake in this example occurred on March 29, 1994 (event 3 in Table 3) as recorded at two stations KIV and ABKT. Station names are shown to the left of the corresponding spectra. In the tests, three layers were assumed with layer thicknesses of 10, 30, and 40 km, overlying a halfspace. The  $Q_\mu$  values in the layers are denoted by  $Q_1$ ,  $Q_2$ ,  $Q_3$ , and  $Q_4$ . In the first test (Figure 21a),  $Q_1$  varies between 30 and 130, with a step of 20.  $Q_2$ ,  $Q_3$ , and  $Q_4$  are fixed at 50, 90,

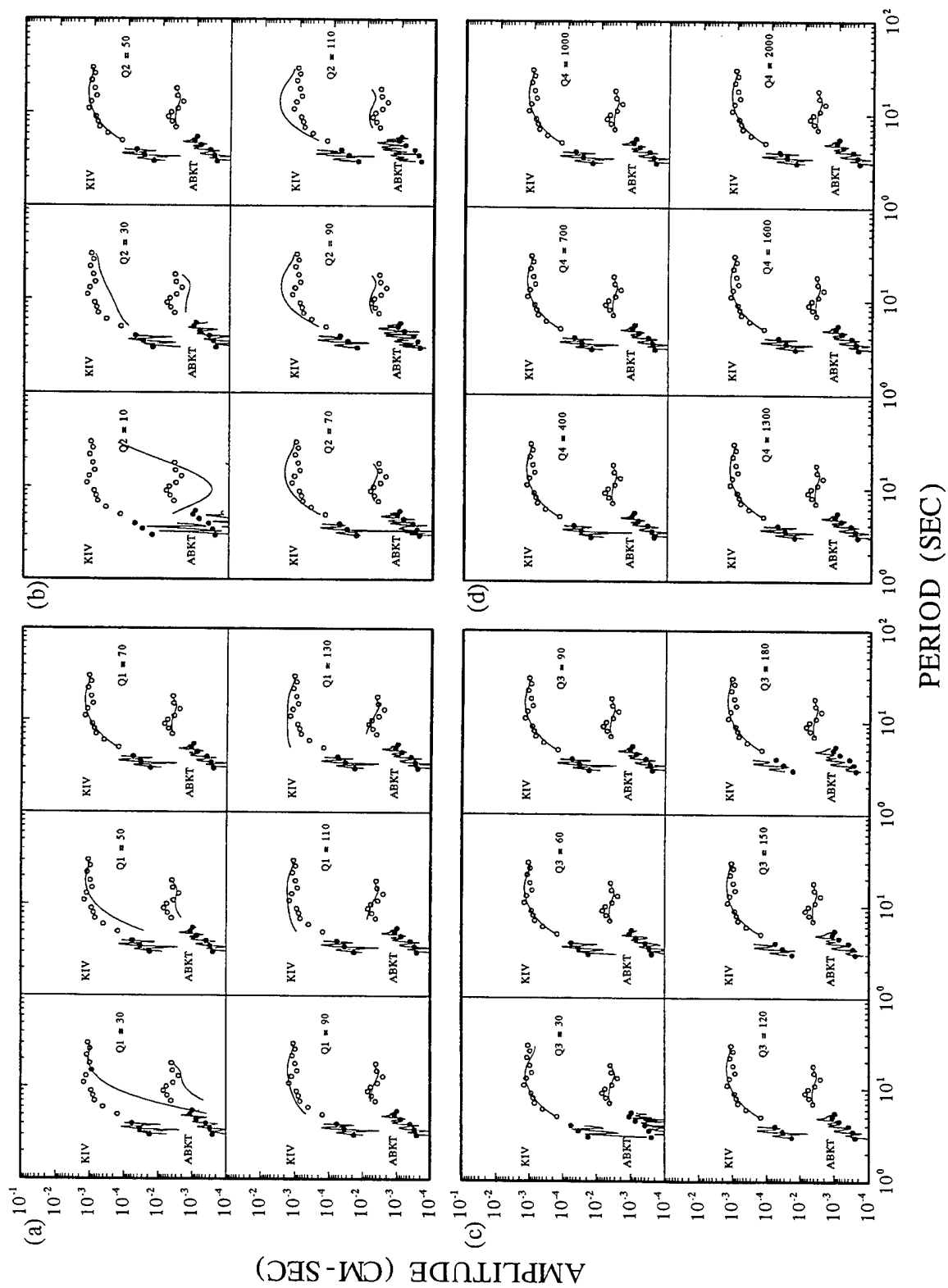


Figure 21

and 700, respectively. These values were inferred from the results obtained using the two-station method. The  $Q_\mu$  value in the halfspace,  $Q_4$ , is somewhat arbitrary since we already know that  $Q_\mu$  cannot be resolved at those depths. As can be seen by comparing the spectra for both stations, the only acceptable solution for  $Q_1$ , among the values shown, is 70. When  $Q_1$  is 90, the fit for the higher modes is good, but at shorter periods theoretical values of the fundamental mode for station KIV are too high.

Figure 21b shows comparisons of the spectra when  $Q_2$  varies. In this test,  $Q_1$  takes the value of 70 as obtained in the previous test.  $Q_3$  and  $Q_4$  were fixed at 90 and 700, respectively.  $Q_2$  varies between 10 and 110 with a step of 20. Both fundamental- and higher-mode spectra are sensitive to the variation of  $Q_2$ . When  $Q_2$  is less than 50, the theoretical curves are lower than observed values for both fundamental and higher modes at the two stations. When  $Q_2$  is greater than 50, the opposite occurs. The only good match occurs when  $Q_2$  is 50.

Figure 21c shows the comparison when  $Q_3$  varies. In this case  $Q_1$  and  $Q_2$  are fixed at 70 and 50, respectively, as determined before, and  $Q_4$  is fixed at 700.  $Q_3$  varies between 30 and 180 with a step of 30. The theoretical curves for the fundamental mode are far less sensitive to the variation of  $Q_3$  than are the higher modes. A good match can be detected when  $Q_3$  takes the values between 60 and 120. A middle value of 90 is therefore chosen as the solution for  $Q_3$ .

In Figure 21d we assign 70, 50 and 90 to  $Q_1$ ,  $Q_2$ , and  $Q_3$ , allowing  $Q_4$  to vary from 400 to 2000. No spectral changes can be detected when  $Q_4$  varies. This indicates that the spectra are not sensitive to changes in  $Q_\mu$  at great depths. No sensitivity to  $Q_\mu$  at depths greater than 80 km was found for any case tested. Therefore, the  $Q_\mu$  models obtained using the single-station method are restricted to the upper 80 km in this study, the same depth range determined in data processing using the two-station method.

The  $Q_\mu$  models for the three regions obtained using the single-station method are listed in Table 4, and superposed on those obtained using the two-

station method (bold lines) as shown in Figure 22. Comparisons of theoretical spectra predicted by the corresponding models with the observed data for all the earthquakes studied in Regions 1, 2, and 3 are presented in Figures 23, 24, and 25, respectively. The events, the recording stations, and models obtained are indicated in the lower right corners of the panels.

**Table 4.**  $Q_\mu$  models obtained using the single-station method

| Layer Number    | Depth (km) | $Q_\mu$ (model 1) | $Q_\mu$ (model 2) | $Q_\mu$ (model 3)                        | $Q_\mu$ (model 4) |
|-----------------|------------|-------------------|-------------------|--|-------------------|
| <i>Region 1</i> |            |                   |                   |  |                   |
| 1               | 0 – 10     | 60                | 70                | 60                                       | 50                |
| 2               | 10 – 40    | 50                | 50                | 60                                       | 50                |
| 3               | 40 – 80    | 90                | 90                | 90                                       | 90                |
| 4               | > 80       | 700               | 700               | 700                                      | 700               |
| <i>Region 2</i> |            |                   |                   |  |                   |
| 1               | 0 – 10     | 60                |                   |  |                   |
| 2               | 10 – 20    | 100               |                   |  |                   |
| 3               | 20 – 40    | 70                |                   |  |                   |
| 4               | 40 – 80    | 120               |                   |  |                   |
| 5               | > 80       | 700               |                   |  |                   |
| <i>Region 3</i> |            |                   |                   |  |                   |
| 1               | 0 – 20     | 180               | 140               | 40 (for 0 – 2 km)<br>180 (for 2 – 20 km) |                   |
| 2               | 20 – 80    | 140               | 140               | 140                                      |                   |
| 3               | > 80       | 700               | 700               | 700                                      |                   |

For events 1 and 3 in Region 1 (Figure 23), two seismograms are available. In general, the match is good for both fundamental-mode and higher-mode spectra for all of the events used. For this region, four models were obtained, indicating that the  $Q_\mu$  models are path dependent. The four models differ only in the crust.  $Q_\mu$  varies between 50 and 70 for the upper 10 km, and between 50 and 60 for the underlying layer (10-40 km). Although the four models differ, they all lie close to the model obtained by the two-station method (bold line). This indicates that the model obtained using the two-station method for this region is applicable and can be thought of as an average model for the region.

One of the advantages of using the single-station method is that the applicable range for the models obtained using the two-station method can be

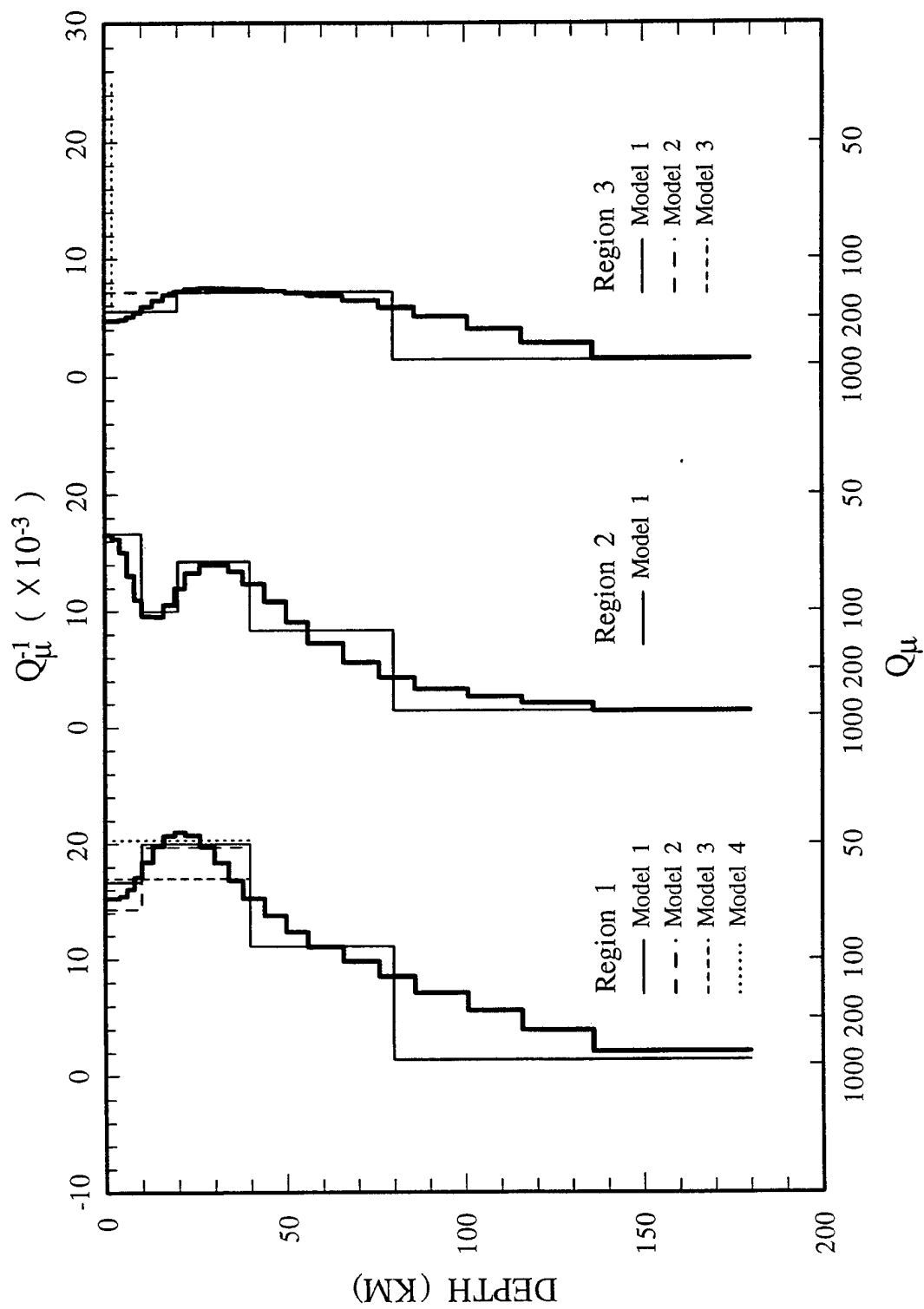
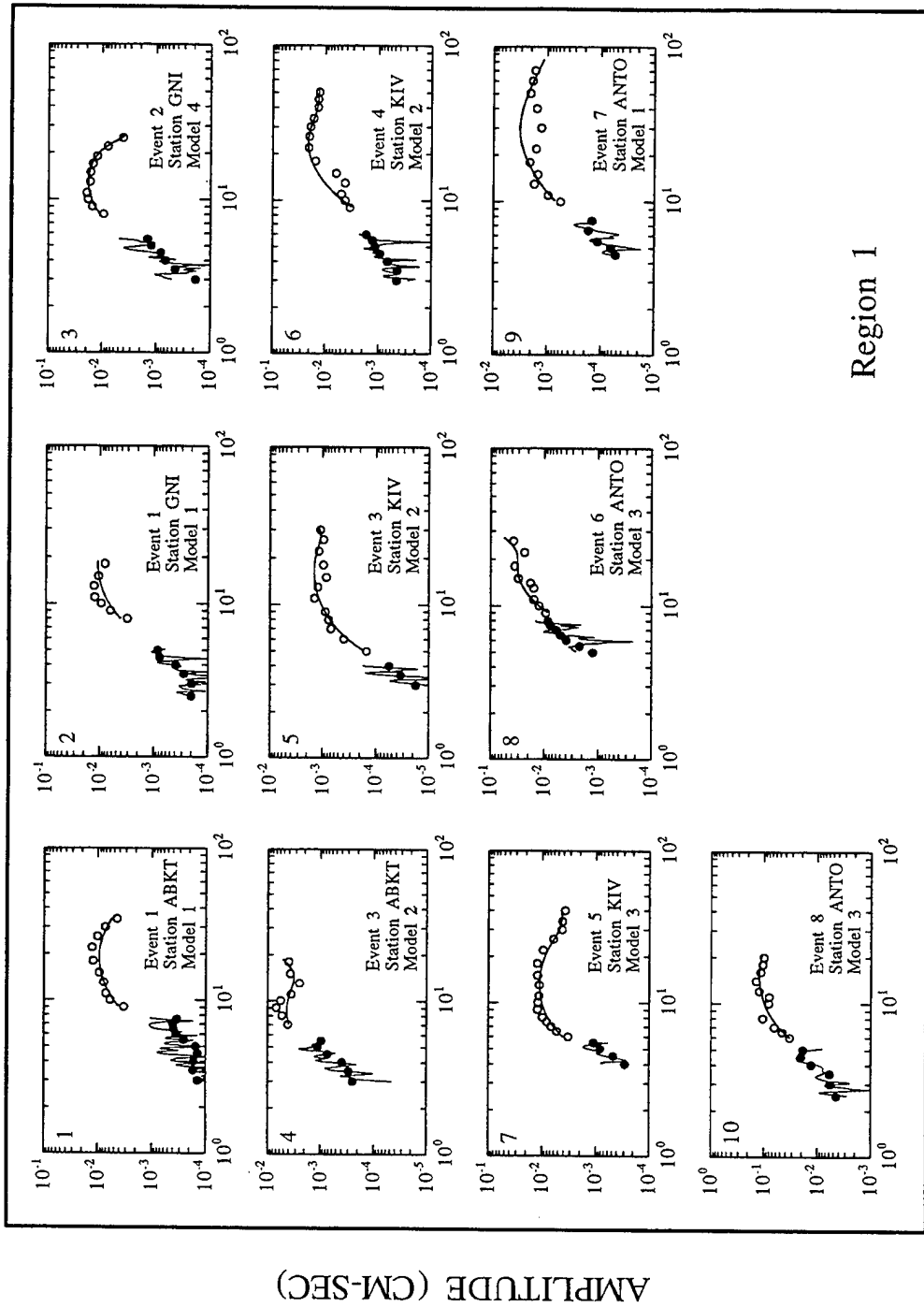


Figure 22





PERIOD (SEC)

Figure 23

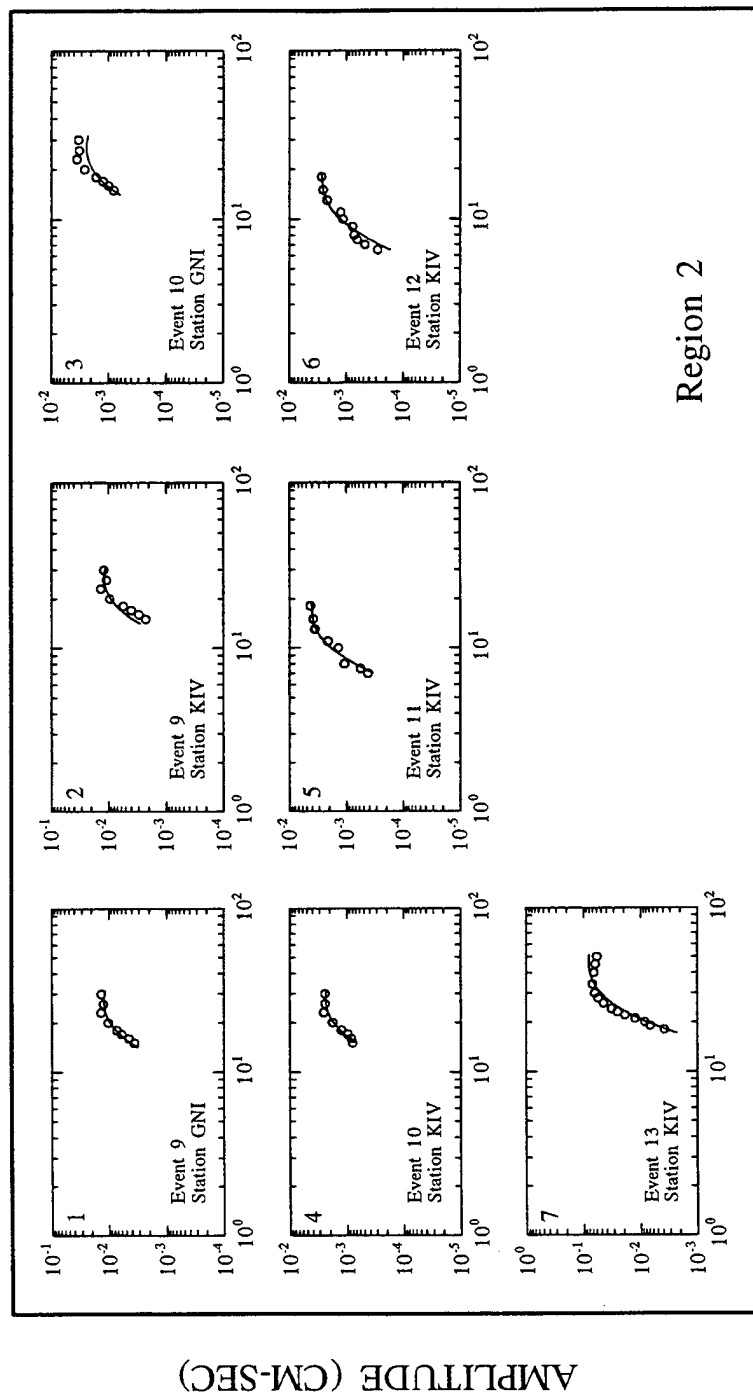
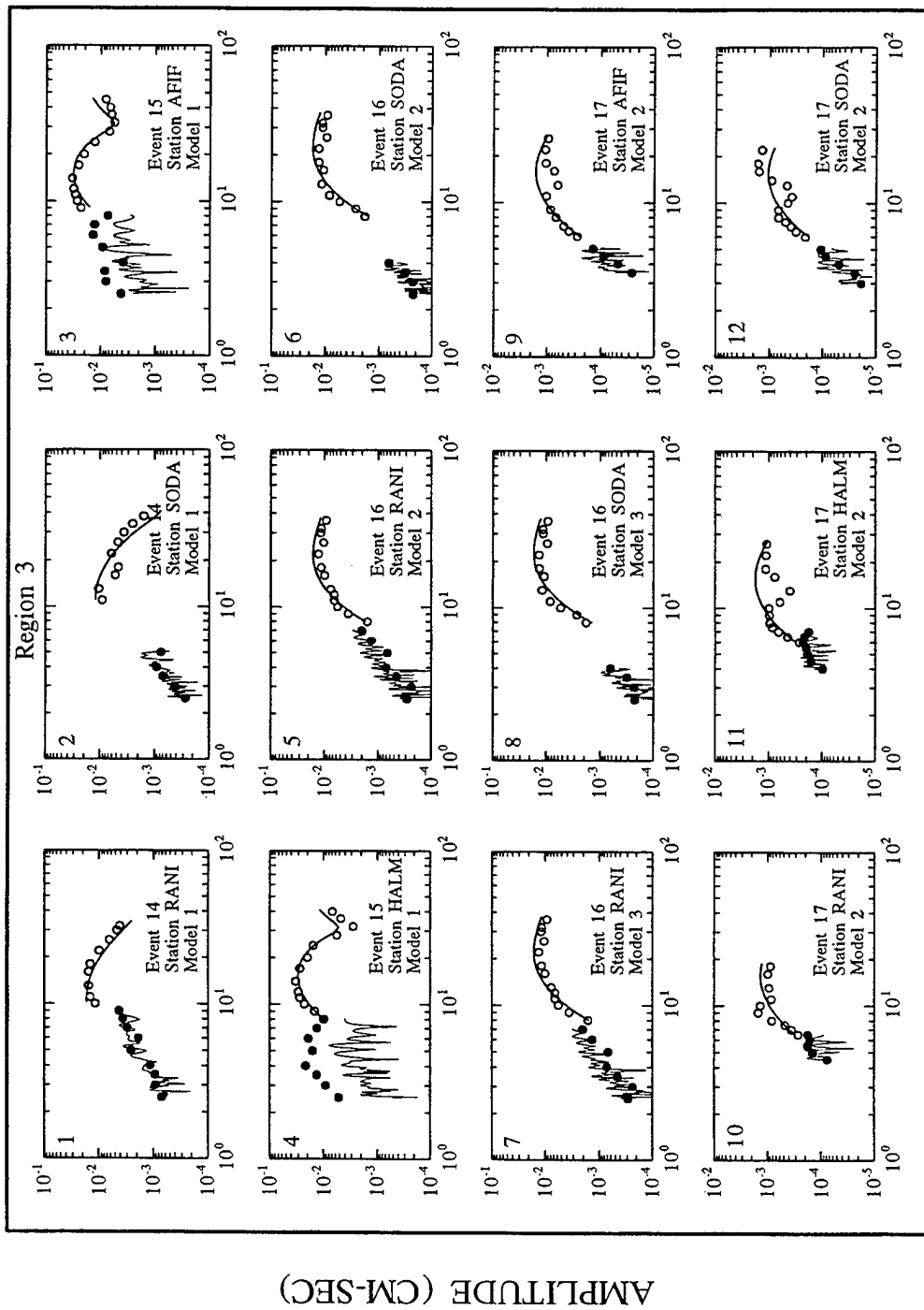


Figure 24



PERIOD (SEC)

Figure 25

broadened. We previously used the station pairs ANTO-GNI and GNI-KIV in Region 1. The results for velocity and  $Q_\mu$  are only valid for the Turkish Plateau or, strictly speaking, the region along the interstation paths. Figure 3 shows that some paths lie in the Iranian Plateau and some paths go through both the Turkish and Iranian Plateaus. This leads us to conclude that the velocity and  $Q_\mu$  models previously obtained for the Turkish Plateau also apply to the Iranian Plateau.

Comparisons of the theoretical and observed spectra for Region 2 are plotted in Figure 24. Five events recorded at stations GNI and KIV were used. Three paths cross the northern portion of the Black Sea, whereas 4 paths cross the Caspian Sea. Events 9 and 10 are recorded at both stations. All paths include both oceanic and continental segments.

The method used for Region 1 is not applicable to Region 2 since no higher-mode spectra were observable for any of the 5 events. In this case, we first simplified the previously obtained model for this region, and computed only the fundamental-mode spectrum. Strictly speaking, the model listed in Table 4 for this region, therefore, is not the one obtained using the single-station method.

Higher-mode energy is probably absent because it cannot propagate through the oceanic crust beneath the Caspian and Black Seas. The model obtained for this region is less unique than models obtained using multimode spectra. Fluctuations in the model may not represent a real feature of the crust, but may be due to systematic errors in the attenuation data caused by the lateral variations of  $Q_\mu$  and velocity in this region.

Five events recorded at 5 stations were used for Region 3 (Figure 25). Events 14 and 15 are located at the southern end of the Dead Sea fault. Paths connecting these two events and stations cross the central and western portions of the peninsula. Event 17 lies in the Gulf of Aden and the path to the station traverses small portion of the Gulf. Most of the paths are in the central and southern part of the peninsula. Event 16 is in the Zagros folded zone. The path from

that event crosses the shield, the shelf, and the basins.

Panels 1 and 2 are for event 14 recorded at stations RANI and SODA, respectively. For this event, model 1 (180 for the upper 20 km and 140 for depth range 20-80 km) was obtained for both of the two paths. Panels 3 and 4 are for event 15, which is located very close to event 14. For this event, the records of two stations (AFIF and HALM) are available for  $Q_\mu$  modeling. Since the paths deviate only slightly from that connecting event 14 and RANI, we tried the same model as for event 14. As shown, the theoretical spectrum for the fundamental mode is in good agreement with the observed data at each station. For higher modes, however, the observed spectra are higher than expected by nearly an order of magnitude. Even using an extremely high  $Q_\mu$  value of 1000 for all of the layers, the synthetics for the higher modes are still lower than the observed spectra. This suggests that the large amplitudes of  $L_g$  in these two records cannot be explained by high  $Q_\mu$  in the crust. Focusing or site effects that affect high-frequency waves coming from northwest of the peninsula might be responsible for the unusual high values of the spectra.

The paths from event 16 to the recording stations SODA and RANI cross basins where a thick cover of low- $Q$  sediment exists.  $Q_\mu$  for those paths (model 2 in Table 4) is 140 for the upper 20 km of the crust. This value is 22% lower than  $Q_\mu$  for model 1. Panels 7 and 8 in Figure 25 show an optional model (model 3) for the same paths as panels 5 and 6. In this model,  $Q_\mu$  in the uppermost 2 km is 40 and in the next 18 km is 180 as in model 1. A model with a 2-km thick layer with a  $Q_\mu$  of 40 can explain the observed spectra in the eastern portion of the Arabian Peninsula. Alternative models can also explain the spectra. One possibility is a 3-km thick layer in which  $Q_\mu$  is 50 and another is a 4-km thick layer in which  $Q_\mu$  is 60. The predicted spectra are nearly identical to those in panels 7 and 8, and are, therefore, not plotted.

Panels 9 through 12 are for event 17 and the recording stations AFIF, RANI, HALM, and SODA, respectively. For those paths, model 2 provides the

best fit to the observed spectra. Since about 20-25% of those paths cross water, we might expect that the best model for the southern portion of the peninsula would be model 1 rather than model 2. The observed spectra, however, exhibit small spectral holes at about 12 sec that are not predicted by the given focal mechanism. This may mean that the reported focal mechanism is incorrect and our  $Q_\mu$  values at shallow depths may be biased too low for this reason.

In general, for the western, central, and southern portions of the Arabian Peninsula, the crust and uppermost mantle can be modeled as a 20-km thick layer with  $Q_\mu$  of 180 and a 60-km thick layer with  $Q_\mu$  of 140. For the eastern portion of the peninsula, the low  $Q$  sediments must be taken into account.  $Q_\mu$  for the sediments can be as low as 40-60.

For Regions 1 and 3, the  $Q_\mu$  models obtained using the two- and single-station methods show good agreement. For Region 2, however,  $Q_\mu$  models are not verified by the single-station method. Since the higher-mode energy was not detected in the observation, we could not vary the  $Q_\mu$  value of any layer, but used the simplified model to compute the theoretical fundamental-mode spectrum and compared it to the observed spectrum. The results are probably less unique than models obtained using multimode spectra. For both methods the paths cross both continental and oceanic areas, that are characterized by different seismic velocity and  $Q_\mu$  distributions. We attempted to model this laterally complex region using one-dimension inversion. We think that the fluctuations in the model may be caused by the lateral complexities of  $Q_\mu$  and velocity, and may not represent the real crustal properties of this region.

Our results indicate that  $Q_\mu$  is higher in the Arabian Peninsula than in the Turkish and Iranian Plateaus. This is consistent with the results obtained from  $L_g$  coda  $Q$  measurements (Cong and Mitchell, 1998). In that study,  $L_g$  coda  $Q$  is low throughout the plateaus, being in the range 150-300. It is higher for much of the peninsula, ranging between 350 and 450. Results of this study show that  $Q_\mu$  is higher in the peninsula than in the plateaus. The average  $Q_\mu$  values for the

uppermost 40 km are 55 and 150 for Regions 1 and 3, respectively. In the  $L_g$  coda  $Q$  study,  $Q$  at 1 Hz varies laterally in the Arabian Peninsula with higher values (about 450) in the shield area, and lower values (about 350) in the platform and basins. In this study, we obtained a  $Q_\mu$  model of 180 for the uppermost 20 km and 140 for the layer 20-80 km for the northern, western, and southern portions of the Arabian Peninsula. If the paths cross the shield, the shelf, and basins, we have to include a low- $Q$  layer in the model to explain the data. This is also in agreement with the results from the  $L_g$  coda  $Q$  study.

## 9. Discussion

Previous studies indicate that  $Q_\mu$  varies regionally, being typically high in stable regions and low in tectonically active regions (Mitchell 1995). The northern portion of the Middle East is characterized by severe deformation and young tectonic features. Continental collision is occurring along the Zagros suture zone, resulting in the Zagros folded belt. The left-lateral East Anatolian fault and right-lateral North Anatolian fault became active 5 Ma. As proposed in recent research (Mitchell, 1995; Mitchell *et al.*, 1997),  $Q_\mu$  and  $Q$  of any wave propagating through the crust in any region are ultimately governed by the type, severity, and temporal occurrence of tectonic activity there. According to that proposal, enhanced temperature associated with tectonic activity has released water of hydration that resides in cracks and permeable rock of the crust, causing low  $Q$  there.

Tectonically active regions are usually characterized by high heat flow. Ilk-isik (1995) recently found that the average heat flow value in western Anatolia is about  $107 \text{ mW m}^{-2}$ , which is about 60% above the world average value. A value as high as  $247 \text{ mW m}^{-2}$  was even measured at a location of  $38^\circ 57' \text{N}$  and  $29^\circ 13.2' \text{E}$ . Wyllie (1988) described ways in which hydrothermal fluids could be generated by elevated temperatures through broad regions of the mantle. In a region of plate convergence, such as Turkey and Iran, those fluids may originate

in a portion of the Arabian plate subducting beneath Eurasian plate. Upper mantle fluids, once released, propagate slowly upward and eventually reside, predominantly, in the crust. The energy used to move fluids through that permeable crust is lost from wave propagating through it, resulting in higher wave attenuation.

Although the  $Q_\mu$  values in the Arabian Shield are higher than those in the northern portion of the Middle East, they are lower than those found for other stable regions of the world. Throughout the entire Middle East lower crust exhibits  $Q_\mu$  values no greater than about 150. This contrasts sharply with results from other continental regions where  $Q_\mu$  increases rapidly with depth at mid-crust depths, usually having values as high as several hundred to a thousand. The Arabian Peninsula has been the site of large-scale uplift and extension with associated volcanic activity. The Afro-Arabian dome began forming in the early Cretaceous and is the result of two or more generating systems that are still active (Almond, 1986). Temperatures beneath the dome are as high as  $900^\circ\text{C}$  at a depth of 40 km and these abnormally high temperatures extend as far as 200 km inland from the Red Sea (McGuire and Bohannon, 1989). The low crustal  $Q$  in the Arabian Peninsula may therefore be due to water released from hydrothermal reactions at those elevated temperatures produced by an upper mantle heat source.

## 10. Conclusions

Shear-wave velocity models were obtained using a two-station method for three regions of the Middle East: the Turkish and Iranian Plateaus (Region 1), a region surrounding and including the Black and Caspian Seas (Region 2), and the Arabian Peninsula (Region 3). The shear-velocity models of the three regions differ mostly in the uppermost 20 km, velocity being fastest in Region 3, and slowest in Region 2. The velocity models for Regions 1 and 3 agree well with those found in other studies in the Middle East. Analysis of the resolving kernels and the



effect of initial values on inversion indicate that our velocity models are valid for at least the upper 120 km of the crust and upper mantle.

$Q_\mu$  models obtained using the two-station method show that  $Q_\mu$  varies both with depth and regionally.  $Q_\mu$  is higher in the relatively stable Arabian Peninsula than in the tectonically active plateau regions in the north by a factor of 2-3.  $Q_\mu$  in the Turkish and Iranian Plateaus is 57 in the upper crust, 54 in the lower crust, and 89 in the upper mantle, whereas  $Q_\mu$  values in the Arabian Peninsula at the same depths are, respectively, 178, 135, and 148. Analysis of the resolving kernels and the effect of initial values on inversion indicate that our  $Q_\mu$  models are only correct for the uppermost 80 km of the crust and upper mantle.

Single-station studies have allowed us to study regional variations of anelastic properties in greater detail than that obtained by two-station studies. For Regions 1 and 3, they support our models obtained using the two-station method. They also show that regional variations in  $Q_\mu$  occur within both Region 1 and Region 3. The differences occur in the uppermost crust where they vary between 50 and 70 in the upper 10 km, between 50 and 60 in the depth range 10-40 km for the Turkish and Iranian Plateaus, and between 140 and 180 in the upper 20 km of the Arabian Peninsula. These results support the idea (Mitchell, 1995) that  $Q_\mu$  in the crust of any region is directly proportional to the length of time that has elapsed since the most recent major tectonic activity there. Our results indicate that zones of plate convergence and regional upper mantle heating are characterized by low  $Q_\mu$  extending from the surface to upper mantle depths. This contrasts with results in stable regions and regions of extension where  $Q_\mu$  increases rapidly at mid-crust depths.

Average  $Q_\mu$  values for both the upper and lower crust in the three regions are lower than those obtained in other continental regions of the world. Since the Middle East is a region of plate convergence in the north and high upper mantle temperature and uplift in Saudi Arabia, fluid-filled cracks may occur at lower crustal depths because metamorphic fluids were recently generated there. With

time, we expect that those fluids will be forced to shallower depths and  $Q_\mu$  at lower crustal depths will become larger.

**Acknowledgments.** We thank the IRIS Data Management Center and the German Geophone Data Center for providing the data used in this study. This research was supported by the U.S. Department of Energy and was monitored by the Phillips Laboratory under contract F19628-95-K-0004.

## References

- Almond, D.C., Geological evolution of the Afro-Arabian dome, *Tectonophysics*, 131, 301-332, 1986.
- Berberian, M., Contribution to the seismotectonics of Iran, II, *Rep. Feol. Surv. Iran*, 39, pp. 516, 1976.
- Brown, G.F., Tectonic map of the Arabian Peninsula, Saudi Arabian Peninsula Map AP-2. *Saudi Arabian Dir. Gen. Miner. Resour.*, 1972.
- Canitez, N., S.B. Ucer, Computer determinations for the fault-plane solutions in and near Anatolia, *Tectonophysics*, 4, 235-244, 1967.
- Cheng, C.C., and B.J. Mitchell, Crustal  $Q$  structure in the United States from multi-mode surface waves, *Bull. Seism. Soc. Am.*, 71, 161-181, 1981.
- Coleman, R.G., Ophiolites. Ancient Oceanic Lithosphere? *Springer-Verlag, Berlin*, pp. 229, 1977.
- Cong, L., and B.J. Mitchell,  $L_g$  coda  $Q$  and its relation to the geology and tectonics of the Middle East, *Pure Appl. Geophys.*, submitted, 1998.
- Ghalib, H., Seismic velocity structure and attenuation of the Arabian plate, *Ph.D. Dissertation, St. Louis University*, pp. 314, 1992.
- Herrin, E.H., and T. Goforth, Phase-matched filters: Application to the study of Rayleigh waves, *Bull. Seism. Soc. Am.*, 67, 1259-1275, 1977.
- Herrmann, R.B., *Computer Programs in Seismology*, User's manual Vol. IV, St. Louis University, Missouri, 1987.
- Ilkisik, O.M., Regional heat flow in western Anatolia using silica temperature estimates from thermal springs, *Tectonophysics*, 244, 175-184, 1995.
- Jih, R.S., and C.S. Lynnes, Re-examination of regional  $L_g$   $Q$  variation in Iranian

- Plateau, in *Proc. 14th Ann. PL/DARPA Seismic Research Symposium, 16-17 September 1992*, edited by J.F. Lewkowicz and M. McPhetres, Phillips Laboratory, 200-206, 1992, PL-TR-92-2210, ADA256711.
- Kadinsky-Cade, K., M. Barazangi, J. Oliver, and B. Isacks, Lateral variations of high-frequency seismic wave propagation at regional distances across the Turkish and Iranian Plateau, *J. Geophys. Res.*, **86**, 9377-9396, 1981.
- Ketin, I., Tectonic units of Anatolia, *Bull. Miner. Res. Explo. Inst. Turk.*, **66**, 23-34, 1966.
- Knopoff, L., and A.A. Fouda, Upper mantle structure under the Arabian Peninsula, *Tectonophysics*, **26**, 121-134, 1975.
- McGuire, A.V., and R.G. Bohannon, Timing of mantle upwelling: Evidence for a passive origin for the Red Sea rift, *J. Geophys. Res.*, **94**, 1677-1682, 1989.
- McKenzie, D.P., Active tectonics of the Mediterranean regions, *Geophys. J. R. Astr. Soc.*, **30**, 109-185, 1972.
- Mindevalli, O., and B.J. Mitchell, Crustal structure and possible anisotropy in Turkey from seismic surface wave dispersion, *Geophys. J.*, **97**, 93-106, 1989.
- Mitchell, B.J., Anelastic structure and evolution of the continental crust and upper mantle from seismic surface wave attenuation, *Rev. Geophys.*, **33**, 441-462, 1995.
- Mitchell, B.J., Y. Pan, J. Xie, and L. Cong,  $L_g$  coda  $Q$  variation and the crustal evolution of Eurasia, *J. Geophys. Res.*, in press, 1997.
- Mokhtar, T.A., and M.M. Al-Saeed, Shear wave velocity structures of the Arabian peninsula, *Tectonophysics*, **230**, 105-125, 1994.
- Niazi, M., Crustal thickness in the Central Saudi Arabian Peninsula, *Geophys. J. R. Astr. Soc.*, **15**, 545-547, 1968.

- Nowroozi, A.A., Focal mechanism of earthquakes in Persia, Turkey, west Pakistan, and Afghanistan and plate tectonics of the Middle East, *Bull. Seism. Soc. Am.*, 62, 823-850, 1972.
- Nuttli, O.W., The excitation and attenuation of seismic crustal phases in Iran, *Bull. Seism. Soc. Am.*, 70, 469-485, 1980.
- Powers, R.W., L.F. Ramirez, C.P. Redmond, and E.L. Elberg, Geology of the Arabian Peninsula - sedimentary geology of Saudi Arabia, *U.S. Geol. Surv., Prof. Pap. 560-D*, pp. 147, 1966.
- Seber, D., and B.J. Mitchell, Attenuation of surface waves across the Arabian peninsula, *Tectonophysics*, 204, 137-150, 1992.
- Seber, D., M. Vallvé, E. Sandvol, D. Steer, and M. Barazangi, Middle East tectonics: applications of geographic information systems (GIS), *GSA Today*, 7, 1-6, 1997.
- Sengör, A.M.C., and W.S.F. Kidd, Post-collisional tectonics of the Turkish and Iranian Plateau and a comparison with Tibet, *Tectonophysics*, 55, 361-376, 1979.
- Stocklin, J., Possible ancient continental margins in Iran, in *Geology of continental Margins*, edited by C. Burk and C. Drake, 873-877, Springer-Verlag, New York, 1974.
- Stoneley, R., The geology of the Kuh-e Dalneshin area of southern Iran, and its bearing on the evolution of southern Tethys, *J. Geol. Soc., London*, 138, 509-526, 1981.
- Wyllie, P.J., Magma genesis, plate tectonics, and chemical differentiation of the Earth, *Rev. Geophys.*, 26, 370-404, 1988.

THOMAS AHRENS  
SEISMOLOGICAL LABORATORY 252-21  
CALIFORNIA INST. OF TECHNOLOGY  
PASADENA, CA 91125

AIR FORCE RESEARCH LABORATORY  
ATTN: VSOE  
29 RANDOLPH ROAD  
HANSKOM AFB, MA 01731-3010  
(2 COPIES)

AIR FORCE RESEARCH LABORATORY  
ATTN: RESEARCH LIBRARY/TL  
5 WRIGHT STREET  
HANSKOM AFB, MA 01731-3004

AIR FORCE RESEARCH LABORATORY  
ATTN: AFRL/SUL  
3550 ABERDEEN AVE SE  
KIRTLAND AFB, NM 87117-5776  
(2 COPIES)

RALPH ALEWINE  
NTPO  
1901 N. MOORE STREET, SUITE 609  
ARLINGTON, VA 22209

MUAWIA BARAZANGI  
INSTOC  
3126 SNEE HALL  
CORNELL UNIVERSITY  
ITHACA, NY 14853

T.G. BARKER  
MAXWELL TECHNOLOGIES  
8888 BALBOA AVE.  
SAN DIEGO, CA 92123-1506

DOUGLAS BAUMGARDT  
ENSCO INC.  
5400 PORT ROYAL ROAD  
SPRINGFIELD, VA 22151

THERON J. BENNETT  
MAXWELL TECHNOLOGIES  
11800 SUNRISE VALLEY DRIVE, STE 1212  
RESTON, VA 22091

WILLIAM BENSON  
NAS/COS  
ROOM HA372  
2001 WISCONSIN AVE. NW  
WASHINGTON DC 20007

JONATHAN BERGER  
UNIVERSITY OF CA, SAN DIEGO  
SCRIPPS INST. OF OCEANOGRAPHY  
IGPP, 0225  
9500 GILMAN DRIVE  
LA JOLLA, CA 92093-0225

ROBERT BLANDFORD  
AFTAC  
1300 N. 17TH STREET  
SUITE 1450  
ARLINGTON, VA 22209-2308

LESLIE A. CASEY  
DEPT. OF ENERGY/NN-20  
1000 INDEPENDENCE AVE. SW  
WASHINGTON DC 20585-0420

CENTER FOR MONITORING RESEARCH  
ATTN: LIBRARIAN  
1300 N. 17th STREET, SUITE 1450  
ARLINGTON, VA 22209

ANTON DAINTY  
HQ DSWA/PMA  
6801 TELEGRAPH ROAD  
ALEXANDRIA, VA 22310-3398

CATHERINE DE GROOT-HEDLIN  
UNIV. OF CALIFORNIA, SAN DIEGO  
INST. OF GEOP. & PLANETARY PHYSICS  
8604 LA JOLLA SHORES DRIVE  
SAN DIEGO, CA 92093

DTIC  
8725 JOHN J. KINGMAN ROAD  
FT BELVOIR, VA 22060-6218 (2 COPIES)

DIANE DOSER  
DEPT OF GEOLOGICAL SCIENCES  
THE UNIVERSITY OF TEXAS AT EL PASO  
EL PASO, TX 79968

MARK D. FISK  
MISSION RESEARCH CORPORATION  
735 STATE STREET  
P.O. DRAWER 719  
SANTA BARBARA, CA 93102-0719

LORI GRANT  
MULTIMAX, INC.  
311C FOREST AVE. SUITE 3  
PACIFIC GROVE, CA 93950

HENRY GRAY  
SMU STATISTICS DEPARTMENT  
P.O. BOX 750302  
DALLAS, TX 75275-0302

I. N. GUPTA  
MULTIMAX, INC.  
1441 MCCORMICK DRIVE  
LARGO, MD 20774

DAVID HARKRIDER  
BOSTON COLLEGE  
INSTITUTE FOR SPACE RESEARCH  
140 COMMONWEALTH AVENUE  
CHESTNUT HILL, MA 02167

THOMAS HEARN  
NEW MEXICO STATE UNIVERSITY  
DEPARTMENT OF PHYSICS  
LAS CRUCES, NM 88003

MICHAEL HEDLIN  
UNIV. OF CALIFORNIA, SAN DIEGO  
SCRIPPS INST. OF OCEANOGRAPHY  
IGPP, 0225  
9500 GILMAN DRIVE  
LA JOLLA, CA 92093-0225

DONALD HELMBERGER  
CALIFORNIA INST. OF TECHNOLOGY  
DIV. OF GEOL. & PLANETARY SCIENCES  
SEISMOLOGICAL LABORATORY  
PASADENA, CA 91125

EUGENE HERRIN  
SOUTHERN METHODIST UNIVERSITY  
DEPARTMENT OF GEOLOGICAL  
SCIENCES  
DALLAS, TX 75275-0395

ROBERT HERRMANN  
ST. LOUIS UNIVERSITY  
DEPT OF EARTH & ATMOS. SCIENCES  
3507 LACLEDE AVENUE  
ST. LOUIS, MO 63103

VINDELL HSU  
HQ/AFTAC/TTR  
1030 S. HIGHWAY A1A  
PATRICK AFB, FL 32925-3002

RONG-SONG JIH  
HQ DSWA/PMA  
6801 TELEGRAPH ROAD  
ALEXANDRIA, VA 22310-3398

THOMAS JORDAN  
MASS. INST. OF TECHNOLOGY  
BLDG 54-918  
77 MASSACHUSETTS AVENUE  
CAMBRIDGE, MA 02139

LAWRENCE LIVERMORE NAT'L LAB  
ATTN: TECHNICAL STAFF (PLS ROUTE)  
PO BOX 808, MS L-175  
LIVERMORE, CA 94551

LAWRENCE LIVERMORE NAT'L LAB  
ATTN: TECHNICAL STAFF (PLS ROUTE)  
PO BOX 808, MS L-208  
LIVERMORE, CA 94551

LAWRENCE LIVERMORE NAT'L LAB  
ATTN: TECHNICAL STAFF (PLS ROUTE)  
PO BOX 808, MS L-202  
LIVERMORE, CA 94551

LAWRENCE LIVERMORE NAT'L LAB  
ATTN: TECHNICAL STAFF (PLS ROUTE)  
PO BOX 808, MS L-195  
LIVERMORE, CA 94551

LAWRENCE LIVERMORE NAT'L LAB  
ATTN: TECHNICAL STAFF (PLS ROUTE)  
PO BOX 808, MS L-205  
LIVERMORE, CA 94551

LAWRENCE LIVERMORE NAT'L LAB  
ATTN: TECHNICAL STAFF (PLS ROUTE)  
PO BOX 808, MS L-200  
LIVERMORE, CA 94551

LAWRENCE LIVERMORE NAT'L LAB  
ATTN: TECHNICAL STAFF (PLS ROUTE)  
PO BOX 808, MS L-221  
LIVERMORE, CA 94551

THORNE LAY  
UNIV. OF CALIFORNIA, SANTA CRUZ  
EARTH SCIENCES DEPARTMENT  
EARTH & MARINE SCIENCE BUILDING  
SANTA CRUZ, CA 95064

ANATOLI L. LEVSHIN  
DEPARTMENT OF PHYSICS  
UNIVERSITY OF COLORADO  
CAMPUS BOX 390  
BOULDER, CO 80309-0309

JAMES LEWKOWICZ  
WESTON GEOPHYSICAL CORP.  
325 WEST MAIN STREET  
NORTHBORO, MA 01532

LOS ALAMOS NATIONAL LABORATORY  
ATTN: TECHNICAL STAFF (PLS ROUTE)  
PO BOX 1663, MS F659  
LOS ALAMOS, NM 87545

LOS ALAMOS NATIONAL LABORATORY  
ATTN: TECHNICAL STAFF (PLS ROUTE)  
PO BOX 1663, MS F665  
LOS ALAMOS, NM 87545

LOS ALAMOS NATIONAL LABORATORY  
ATTN: TECHNICAL STAFF (PLS ROUTE)  
PO BOX 1663, MS C335  
LOS ALAMOS, NM 87545

GARY MCCARTOR  
SOUTHERN METHODIST UNIVERSITY  
DEPARTMENT OF PHYSICS  
DALLAS, TX 75275-0395

KEITH MCLAUGHLIN  
CENTER FOR MONITORING RESEARCH  
SAIC  
1300 N. 17TH STREET, SUITE 1450  
ARLINGTON, VA 22209

BRIAN MITCHELL  
DEPT OF EARTH & ATMOS. SCIENCES  
ST. LOUIS UNIVERSITY  
3507 LACLEDE AVENUE  
ST. LOUIS, MO 63103

RICHARD MORROW  
USACDA/IVI  
320 21ST STREET, N.W.  
WASHINGTON DC 20451

JOHN MURPHY  
MAXWELL TECHNOLOGIES  
11800 SUNRISE VALLEY DRIVE, STE 1212  
RESTON, VA 22091

JAMES NI  
NEW MEXICO STATE UNIVERSITY  
DEPARTMENT OF PHYSICS  
LAS CRUCES, NM 88003

ROBERT NORTH  
CENTER FOR MONITORING RESEARCH  
1300 N. 17th STREET, SUITE 1450  
ARLINGTON, VA 22209

OFFICE OF THE SECRETARY OF DEFENSE  
DDR&E  
WASHINGTON DC 20330

JOHN ORCUTT  
INST. OF GEOPH. & PLANETARY PHYSICS  
UNIV. OF CALIFORNIA, SAN DIEGO  
LA JOLLA, CA 92093

PACIFIC NORTHWEST NAT'L LAB  
ATTN: TECHNICAL STAFF (PLS ROUTE)  
PO BOX 999, MS K6-48  
RICHLAND, WA 99352

PACIFIC NORTHWEST NAT'L LAB  
ATTN: TECHNICAL STAFF (PLS ROUTE)  
PO BOX 999, MS K6-40  
RICHLAND, WA 99352

PACIFIC NORTHWEST NAT'L LAB  
ATTN: TECHNICAL STAFF (PLS ROUTE)  
PO BOX 999, MS K6-84  
RICHLAND, WA 99352

PACIFIC NORTHWEST NAT'L LAB  
ATTN: TECHNICAL STAFF (PLS ROUTE)  
PO BOX 999, MS K5-12  
RICHLAND, WA 99352

FRANK PILOTTE  
HQ AFTAC/TT  
1030 S. HIGHWAY A1A  
PATRICK AFB, FL 32925-3002

KEITH PRIESTLEY  
DEPARTMENT OF EARTH SCIENCES  
UNIVERSITY OF CAMBRIDGE  
MADINGLEY RISE, MADINGLEY ROAD  
CAMBRIDGE, CB3 0EZ UK

JAY PULLI  
BBN SYSTEMS AND TECHNOLOGIES, INC.  
1300 NORTH 17TH STREET  
ROSSLYN, VA 22209

DELAINE REITER  
AFRL/VSOE (SENCOM)  
29 RANDOLPH ROAD  
HANSCOM AFB, MA 01731-3010

PAUL RICHARDS  
COLUMBIA UNIVERSITY  
LAMONT-DOHERTY EARTH OBSERV.  
PALISADES, NY 10964

MICHAEL RITZWOLLER  
DEPARTMENT OF PHYSICS  
UNIVERSITY OF COLORADO  
CAMPUS BOX 390  
BOULDER, CO 80309-0309

DAVID RUSSELL  
HQ AFTAC/TTR  
1030 SOUTH HIGHWAY A1A  
PATRICK AFB, FL 32925-3002

CHANDAN SAIKIA  
WOODWARD-CLYDE FED. SERVICES  
566 EL DORADO ST., SUITE 100  
PASADENA, CA 91101-2560

SANDIA NATIONAL LABORATORY  
ATTN: TECHNICAL STAFF (PLS ROUTE)  
DEPT. 5704  
MS 0979, PO BOX 5800  
ALBUQUERQUE, NM 87185-0979

SANDIA NATIONAL LABORATORY  
ATTN: TECHNICAL STAFF (PLS ROUTE)  
DEPT. 9311  
MS 1159, PO BOX 5800  
ALBUQUERQUE, NM 87185-1159

SANDIA NATIONAL LABORATORY  
ATTN: TECHNICAL STAFF (PLS ROUTE)  
DEPT. 5704  
MS 0655, PO BOX 5800  
ALBUQUERQUE, NM 87185-0655

SANDIA NATIONAL LABORATORY  
ATTN: TECHNICAL STAFF (PLS ROUTE)  
DEPT. 5736  
MS 0655, PO BOX 5800  
ALBUQUERQUE, NM 87185-0655

THOMAS SERENO, JR.  
SAIC  
10260 CAMPUS POINT DRIVE  
SAN DIEGO, CA 92121

AVI SHAPIRA  
SEISMOLOGY DIVISION  
IPRG  
P.O.B. 2286  
NOLON 58122 ISRAEL

ROBERT SHUMWAY  
410 MRAK HALL  
DIVISION OF STATISTICS  
UNIVERSITY OF CALIFORNIA  
DAVIS, CA 95616-8671

MATTHEW SIBOL  
ENSCO, INC.  
445 PINEDA CT.  
MELBOURNE, FL 32940

DAVID SIMPSON  
IRIS  
1200 NEW YORK AVE., NW  
SUITE 800  
WASHINGTON DC 20005

JEFFRY STEVENS  
MAXWELL TECHNOLOGIES  
8888 BALBOA AVE.  
SAN DIEGO, CA 92123-1506

BRIAN SULLIVAN  
BOSTON COLLEGE  
INSITUTE FOR SPACE RESEARCH  
140 COMMONWEALTH AVENUE  
CHESTNUT HILL, MA 02167

TACTEC  
BATTELLE MEMORIAL INSTITUTE  
505 KING AVENUE  
COLUMBUS, OH 43201 (FINAL REPORT)

NAFI TOKSOZ  
EARTH RESOURCES LABORATORY, M.I.T.  
42 CARLTON STREET, E34-440  
CAMBRIDGE, MA 02142

LAWRENCE TURNBULL  
ACIS  
DCI/ACIS  
WASHINGTON DC 20505

GREG VAN DER VINK  
IRIS  
1200 NEW YORK AVE., NW  
SUITE 800  
WASHINGTON DC 20005

FRANK VERNON  
UNIV. OF CALIFORNIA, SAN DIEGO  
SCRIPPS INST. OF OCEANOGRAPHY  
IGPP, 0225  
9500 GILMAN DRIVE  
LA JOLLA, CA 92093-0225

TERRY WALLACE  
UNIVERSITY OF ARIZONA  
DEPARTMENT OF GEOSCIENCES  
BUILDING #77  
TUCSON, AZ 85721

JILL WARREN  
LOS ALAMOS NATIONAL LABORATORY  
GROUP NIS-8  
P.O. BOX 1663  
LOS ALAMOS, NM 87545 (5 COPIES)

DANIEL WEILL  
NSF  
EAR-785  
4201 WILSON BLVD., ROOM 785  
ARLINGTON, VA 22230

RU SHAN WU  
UNIV. OF CALIFORNIA SANTA CRUZ  
EARTH SCIENCES DEPT.  
1156 HIGH STREET  
SANTA CRUZ, CA 95064

JIAKANG XIE  
COLUMBIA UNIVERSITY  
LAMONT DOHERTY EARTH OBSERV.  
ROUTE 9W  
PALISADES, NY 10964

JAMES E. ZOLLWEG  
BOISE STATE UNIVERSITY  
GEOSCIENCES DEPT.  
1910 UNIVERSITY DRIVE  
BOISE, ID 83725